Advances in Colloid and Interface Science 146 (2009) 1–17

Contents lists available at ScienceDirect

Advances in Colloid and Interface Science

journal homepage: www.elsevier.com/locate/cis

Quantitative imaging of colloidal flows

Rut Besseling [a,*], Lucio Isa [a], Eric R. Weeks [b], Wilson C.K. Poon [a]

[a] SUPA (Scottish Universities Physics Alliance) and School of Physics & Astronomy, The University of Edinburgh, Kings Buildings, Mayfield Road, Edinburgh EH9 3JZ, United Kingdom
[b] Physics Department, Emory University, Atlanta, Georgia 30322, USA

ARTICLE INFO

Available online 9 October 2008

PACS:
83.80.Hj
83.50.Ha
83.60.La
64.70.Pf
61.20.Ne
61.43.Fs
82.70.Dd

Keywords:
Colloids
Suspensions
Confocal microscopy
Particle tracking
Flow
Rheology

ABSTRACT

We present recent advances in the instrumentation and analysis methods for quantitative imaging of concentrated colloidal suspensions under flow. After a brief review of colloidal imaging, we describe various flow geometries for two and three-dimensional (3D) imaging, including a 'confocal rheoscope'. This latter combination of a confocal microscope and a rheometer permits simultaneous characterization of rheological response and 3D microstructural imaging. The main part of the paper discusses in detail how to identify and track particles from confocal images taken during flow. After analyzing the performance of the most commonly used colloid tracking algorithm by Crocker and Grier extended to flowing systems, we propose two new algorithms for reliable particle tracking in non-uniform flows to the level of accuracy already available for quiescent systems. We illustrate the methods by applying it to data collected from colloidal flows in three different geometries (channel flow, parallel plate shear and cone plate rheometry).

Contents

1. Introduction . . . 2
2. Imaging colloidal suspensions . . . 2
3. Materials and instrumentation . . . 3
   3.1. The colloidal particles . . . 3
   3.2. The confocal microscope . . . 4
   3.3. Shear cell . . . 5
   3.4. Capillary flow . . . 5
   3.5. Confocal rheoscope . . . 6
4. Particle location and its limitations . . . 6
   4.1. Locating and identifying the particles . . . 6
   4.2. Limitations . . . 6
5. Tracking algorithms . . . 7
   5.1. The classic CG algorithm . . . 7
      5.1.1. Tracking algorithm . . . 7
      5.1.2. Hard particle simulations . . . 7
      5.1.3. Quiescent system . . . 8
      5.1.4. 2D system in shear flow . . . 8
      5.1.5. Summary of evaluation of CG tracking . . . 8
   5.2. Iterated CG tracking algorithm . . . 9
      5.2.1. Description . . . 9
      5.2.2. Uniformly moving system . . . 9

* Corresponding author.
E-mail address: rbesseli@ph.ed.ac.uk (R. Besseling).

0001-8686/$ – see front matter © 2008 Elsevier B.V. All rights reserved.
doi:10.1016/j.cis.2008.09.008

5.3. Correlated image tracking . . . 10
5.3.1. Description . . . 10
5.3.2. Limitations of correlated image tracking . . . 11
6. Applications . . . 12
6.1. 2D tracking of channel flows . . . 13
6.2. 3D particle tracking in simple shear flow . . . 14
6.3. Rheology and velocity profiling . . . 15
7. Conclusion . . . 16
Acknowledgements . . . 16
References . . . 16

1. Introduction

The last two decades have seen a surge of interest in the behavior of concentrated colloidal suspensions. These systems have long attracted attention because of their evident practical importance. However, developments since the 1980s have shown that well-characterized colloidal suspensions, in which the size, shape and interaction of the particles are known, can serve as experimental model systems for understanding generic phenomena in condensed systems. Initially, this 'colloids as big atoms' approach has focussed on the use of model colloids to study equilibrium phenomena in the bulk such as liquid structure and phase behavior [1–3]. Since then, interfacial phenomena have been investigated [4], as well as bulk non-equilibrium phenomena such as phase transition kinetics [5], glassy arrest [6,7] and gelation [8]. In all cases, the well-characterized nature of the experimental systems has meant that very direct comparison with theory and simulations are possible; such synergism gives rise to rapid advances in understanding.

Most recently, the spotlight has been on the use of model colloids to study *driven* non-equilibrium phenomena. In particular, coincident with intense developments in a variety of theoretical approaches [9–11], colloids are increasingly seen as model systems for studying the rheology of arrested matter. Here, perhaps more so than previously, fundamental interest and immediate industrial relevance directly coincide. Concentrated particulate suspensions, sometimes known as pastes, have widespread applications [12], most (if not all) of which will involve the suspensions being mechanically driven far away from equilibrium either as part of processing (e.g. in ceramics manufacture [13]) and/or during use. Here, as before, the study of well-characterized colloids can yield fundamental insights, many of which are likely applicable to 'real' systems with little need of 'translation'. Moreover, we may expect that driven colloidal suspensions can, in some respects, be similar to driven granular materials, themselves the focus of intense study for both fundamental and applied reasons [14]. Quantitative similarities of this kind have indeed been found recently for the case of channel flow [15]. If more such analogies are found in the future, a unified description of colloids and grains may indeed be possible [16].

The elucidation of structure and dynamics have always been important goals in the study of colloids in general, and of model colloids in particular. Traditionally, structural and dynamical information in this and other areas of soft matter science is derived from scattering [17]. The outputs from such experiments are the static and dynamic structure factors. These average quantities are often directly calculable from theory, which partly explains the appeal of scattering methods in the first place.

But the upper range of the colloidal length scale is in the optical domain, and so is amenable to direct imaging in an optical microscope. Given the centrality of imaging in Perrin's pioneering (and Nobel Prize winning) work using colloids to prove the existence of atoms [18], it is at first sight surprising that optical imaging played almost no further role in the study of colloids until the last two decades of the 20th century. But the imaging of all but the most dilute suspensions had to await two developments.

First, model systems are needed in which the refractive index of the particles can be closely, if not perfectly, matched to that of the surrounding solvent; otherwise concentrated suspensions of large particles that are in principle optically resolvable are turbid, and thus not amenable to optical imaging. A number of such systems have been developed since the 1980s. (The development of such systems also benefits the use of light scattering, which also requires index matching.) Secondly, an imaging method needs to be found that can deal with at least a certain degree of translucency in samples. Such a method, confocal microscopy, was invented (and patented) by Marvin Minsky in 1955. The development of the methodology in the first few decades since its invention was driven largely by the requirements of biologists. Since the mid-1990s, however, there has been a surge in interest in applying confocal microscopy to the study of model concentrated colloidal suspensions. Initially, this interest was focussed on *quiescent* systems [19]. In the last few years, however, it has been demonstrated that confocal microscopy can also be used with profit to study *flowing* colloids, and thus yield unique insights into the rheology of pastes. The purpose of this work is to set out in detail, for the first time, how this can be done.

The rest of the paper is organized as follows. We first briefly review the use of imaging methods to study colloids. We then describe in Section 3 new hardware that we have developed to image colloidal flows in various geometries. In Section 4 we review the basics of feature identification in (confocal) images and discuss various limits to particle identification in 2D and 3D flow fields. The core of the work is Section 5, where we turn to particle tracking. In Section 5.1 we evaluate for the first time, using data from simulations, the applicability of a classic (and widely applied) tracking algorithm [20] in quiescent and sheared systems where the average motion is zero. We then describe in detail, Sections 5.2 and 5.3, our new methods to track particles in the presence of flow. Finally, in Section 6 we demonstrate the applicability of these methods to imaging colloidal flows in various geometries, including home built environments and a commercial rheometer.

2. Imaging colloidal suspensions

The imaging of a single layer of colloids has been used to great effect to study fundamental processes in 2D as illustrated for example by the work of Maret and co-workers e.g. [21–23]). Despite being less problematic than three-dimensional imaging, 2D (bright-field) imaging may nonetheless have its specific challenges, e.g. when analyzing imaged objects that have come into very close proximity [24].

The use of conventional (non-confocal) optical microscopy to study concentrated colloidal suspensions in 3D has been reviewed before [25]. In nearly index-matched suspensions, contrast is generated using either phase contrast or differential interference contrast (DIC) techniques. One advantage of conventional microscopy is speed: image frames can easily be acquired at video rate. But it has poor 'optical sectioning' due to the presence of significant out-of-focus information, so that particle coordinates in concentrated systems cannot be reconstructed in general, although structural information is still obtainable under special circumstances [26].

Compared to conventional microscopy, confocal microscopy delivers superior optical sectioning by using a pinhole in a plane conjugate with the focal (*xy*) plane. It allows a crisp 3D image to be built up from a stack of 2D images. But each 2D image needs to be acquired by scanning, which imposes limits on its speed. The technique has been described in detail before [27].

The use of confocal microscopy in the study of concentrated colloidal suspensions was pioneered by van Blaaderen and Wiltzius [28], who showed that the structure of a random-close-packed sediment could be reconstructed at the single particle level. Confocal microscopy of colloidal suspensions in the absence of flow has been reviewed recently [19,29–31], and we refer the reader to these reviews for details and references. Here, we simply note that this methodology gives direct access to *local* processes, such as crystal nucleation [32] and dynamic heterogeneities in hard-sphere suspensions near the glass transition [33,34].

In this work, we focus on the use of confocal microscopy for imaging colloids *under flow*, or confocal rheo-imaging (reviewed in [35]). Conventional rheology studies the mechanical response of bulk samples. As far as the study of concentrated, model suspensions is concerned, much attention has been given in the last few years to *non-linear* rheological phenomena, e.g., the different ways in which repulsion- and attraction-dominated colloidal glasses yield [36,37]. The bulk rheological data are consistent with the former yielding by a single-step process of cage breaking, and the latter yielding in two steps, first breaking interparticle bonds, and then breaking nearest-neighbor cages. Confocal imaging can play a decisive role in the verification of such microscopic interpretation, which inevitably makes reference to local processes on the single-particle level. Moreover, direct imaging can clearly shed light on complicating factors in conventional rheological measurements such as wall slip [38,39] and flow non-uniformities such as shear banding [40]. Here, significant progress can be made without imaging at single-particle resolution, by using various coarse-grained velocimetry methods. Traditional Particle Image Velocimetry (PIV) [41] requires transparent samples. This technique has recently been used in a rheometer to give important information on slip in emulsions [42,43].

Other methods for velocimetry with no requirement for transparency have been developed, such as heterodyne light-scattering [44] and ultrasonic velocimetry [45]. The latter has been applied to characterize slip and flow nonlinearities in micelles and emulsions [46,47].

A robust method for velocimetry which can also provide additional information on the density profiles is Nuclear Magnetic Resonance Imaging (NMRI) [48–51]. The technique has spatial resolution down to ~20 μm and has been combined with rheometric setups to relate velocity profiles to macroscopic rheology [52,53]. This approach has been used to investigate the occurrence of shear bands [54] and shear thickening [55].

Thus, both PIV and NMRI give additional insight unavailable from bulk rheology alone. But to build up a complete picture of colloidal flow, it is desirable also to have information on the single particle level. For this purpose, a method related to PIV and particle tracking has been applied to non-Brownian suspensions and allowed the measurement of non-affine particle motion and diffusivity [56,57]. But *direct* imaging of the microstructure during flow is needed to give complete microstructural information. Optical microscopy has this capability.

It is possible to use conventional (non-confocal) video microscopy to study shear effects in 3D [58–61]. But the poor optical sectioning hinders complete, quantitative image analysis. Confocal microscopy significantly improves sectioning, and permits in principle the extraction of particle coordinates. But the need for scanning initially meant rather slow data acquisition rates, so that observations in real time (i.e. during shear) produced blurred images that again limited the potential for quantitative analysis [62]. A common solution was to apply shear, and then image immediately after the cessation of shear, both in 2D [63,64] and in 3D [62,65–67]. (Earlier work using conventional video microscopy [58,59] resorted to the same strategy.)

More recently, the availability of fast confocal systems (see Section 3.2) means that nearly-real-time reconstruction of structure during flow in 3D at single-particle resolution has become possible. Such experiments face two key challenges: sample environment and data analysis. First, the flow geometry used clearly must be compatible with the optical requirements of simultaneous confocal imaging. A number of different arrangements have been demonstrated to date. Derks et al. carried out a first experimental study by using a counter-rotating cone and plate shear cell combined with a fast confocal microscope [68] and obtained particle coordinates and tracks in the zero-velocity plane as well as velocity profiles across the geometry gap. The same group has recently produced a more sophisticated set up which uses a parallel plate shear cell [69] capable of spanning a vast range of shear rates and frequencies which they used to study crystallization of colloids under shear. A parallel plate shear cell has also been used by Besseling et al. [70] to study the shear-induced relaxation in hard-sphere colloidal glasses, while recent experiments by Isa et al. [15] have elucidated the behavior of colloidal sediments flowing into micro-channels. In this work, we give the details for two of these geometries [15,70], and describe and demonstrate a new one: the coupling of a fast confocal scanner to a commercial rheometer, which allows simultaneous confocal imaging and full rheological characterization of the same sample.

The second challenge is data analysis: how to extract accurate particle coordinates from raw image stacks. In particular, special methods are needed for reliable tracking, since the large displacements from frame to frame imposed by flow may inhibit correct identification of particles between frames. The same problem confronts the use of imaging to study granular flows [71]. In this work, we describe in detail a new method for tracking particles from confocal images acquired during flow. We demonstrate its correctness and measure its limitations by using data from computer simulations, as well as illustrate its use with real experimental data.

3. Materials and instrumentation

3.1. The colloidal particles

Our goal is to perform confocal imaging in real time at single-particle resolution of colloidal suspensions under flow. Confocal microscopy is, in principle, able to image inside slightly turbid systems, but the image quality deteriorates with sample turbidity. In order to obtain sharp images as possible to test the limits of our methodology, we performed experiments using an index-matched suspension that is optically clear.

The particles were poly-methyl-methacrylate (PMMA) spheres, sterically-stabilized by chemically-grafted poly-12-hydroxy stearic acid (PHSA) [72]. The particles can be dyed with a fluorophore (NBD, 4 chloro-7 nitrobenz-2 oxa 1,3 diazole), which is excited at 488 nm and emits at 525 nm. Particles can be suspended in a mixture of decalin (mixed-decahydronaphtalene, Sigma-Aldrich, $n_{\mathrm{decalin}} = 1.4725 \pm 0.0005$) and tetralin (tetrahydronaphtalene, Sigma-Aldrich, $n_{\mathrm{tetralin}} \simeq 1.5410 \pm 0.0005$) to achieve full refractive index matching of the solvent and the particles ($n_{\mathrm{susp}} \simeq 1.5$). This matching ensures hard-spheres interactions [73] and also limits scattering of both the laser and the excited light during confocal microscopy. However, the decalin–tetralin mixture has a lower density than PMMA (1.88 g/cm^3). To achieve buoyancy-matching, particles can be suspended in a mixture of cyclo-heptyl-bromide (CHB) and mixed-decalin [74]. The buoyancy-matching composition also closely matches the refractive index of the suspension ($n_{\mathrm{susp}} = 1.494$) [29]. The addition of CHB to a hard-spheres suspension induces charge on the particles, which can be screened by adding a suitable amount (4 mM) of salt [74] (tetrabutylammonium chloride, $(C_4H_9)_4NCL$, $M_W = 277.92$ g, Fluka).

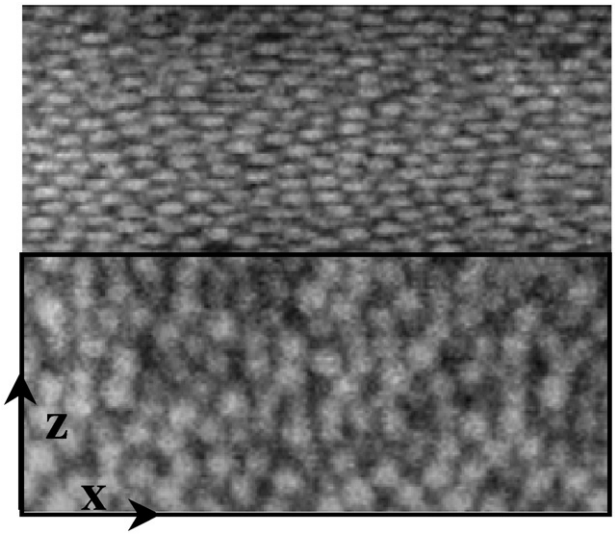

Fig. 1. Projection of a raw 3D image stack of $x \times y \times z \sim 29 \times 29 \times 15\ \mu m^3$ (256×256×76 voxels) taken in ~1 s. The particle radius is 850 nm.

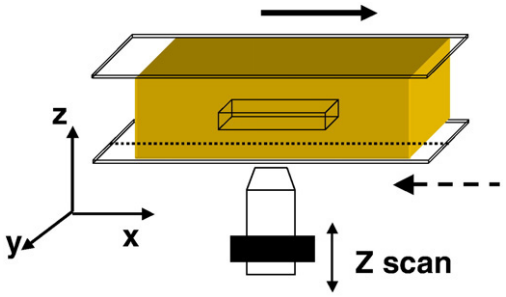

Fig. 2. Sketch of the shear cell. The sample is positioned between two parallel slides; the top one is driven by a mechanical actuator while the bottom one can either be fixed or be translated in the opposite direction (dashed arrow). The suspension is imaged from below (image volume highlighted) with a confocal microscope the focal depth of which is controlled by a piezo-electric element.

The buoyancy-matching is very sensitive to temperature changes; the thermal expansion coefficient of the solvent exceeds that of PMMA by about a factor ten and a decalin–CHB mixture of a given composition will therefore match the particle density only in a very narrow temperature range [75]. We exploit this fact to prepare suspensions of different volume fractions by centrifuging the suspension at a temperature $T \geq 35$ °C, above the buoyancy matching temperature, to create a sediment which can subsequently be diluted. Finally, imaging can either be performed on a fully fluorescent sample or on refractive index-matched systems seeded with fluorescent particles. In the course of our description we shall specify the details of the system used in each example.

3.2. The confocal microscope

To perform confocal imaging during flow, high acquisition rates and thus fast laser scanning methods are required. Among these are spinning disk systems [27] (with possible micro-lens array extension) or laser scanning by resonant galvanometric mirrors. The confocal scanner we use (VT-Eye, Visitech International, with a solid state 488 nm laser) employs a combination of a standard galvanometer and an acousto-optic deflector (AOD)[1]. The former positions the laser beam at a certain y-position, while the AOD much more rapidly scans a line along x. The acquisition rate is thus mainly determined by the 'slow' galvanometer. Typical frame rates for 2D image series range from $f_{scan} = 5$ Hz for images of 1024×1024 pixels to $f_{scan} = 100$–200 Hz for images of 256×256 pixels. The upper limits on colloid diffusivity or flow speed imposed by these acquisition rates are described in Section 4.2.

We have imaged flow in a parallel plate shear cell and in square capillaries using the 'standard configuration', where the confocal scanner is coupled to a Nikon TE Eclipse 300 inverted microscope, with a 100× or 60× magnification, oil-immersion objective with a numerical aperture (NA) of 1.4. The depth of the focal plane, z, is controlled by a piezo-element mounted on the microscope nosepiece. For 3D imaging, a z-stack of 2D images is collected (Fig. 1) by rapid variation of the height of the piezo and synchronized 2D acquisition at each z. The corresponding 3D acquisition time is N_z/f_{scan} with N_z the number of 2D slices. We have also coupled the confocal scanner to a

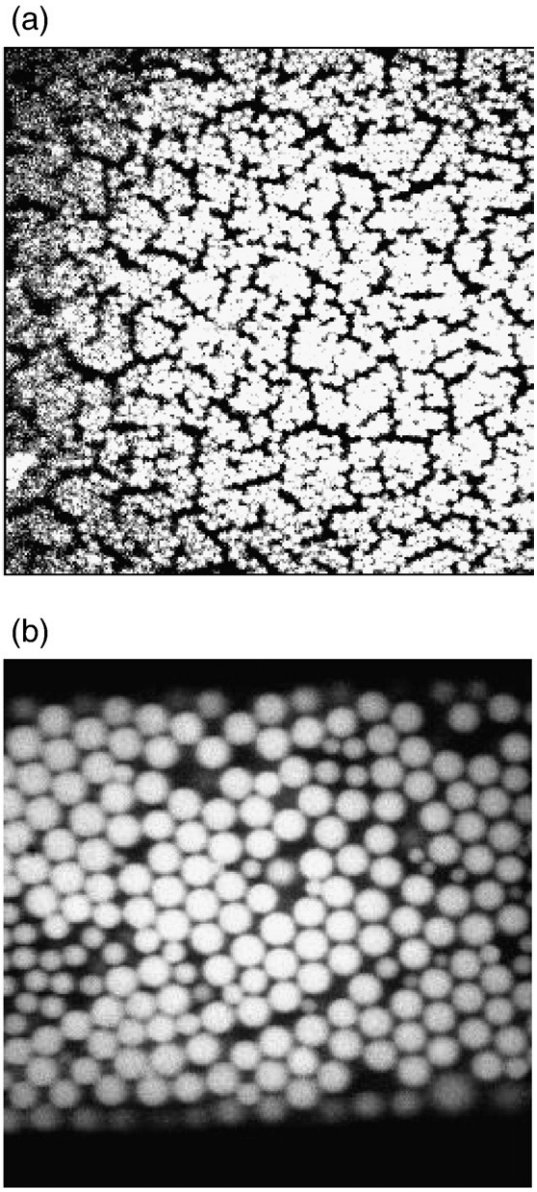

Fig. 3. Confocal images of the coating (a) on a cover slide for shear flow imaging (image size: 56 µm×56 µm), (b) on the inner surface of a 50 µm×50 µm glass capillary (image size: 43 µm×43 µm. The larger particles in (b) form the coating, the smaller ones are suspended and flowing.

[1] To accommodate the wavelength dependent deflection of the AOD, the instrument uses a slit instead of a pinhole, but in practice the resolution is very similar to that of standard pinhole configuration.

commercial rheometer, to enable simultaneous imaging and rheological measurements on the same sample.

3.3. Shear cell

Initial experiments on shear flow were performed with a linear parallel plate shear cell (plate separation $Z_{gap} \sim 400$–800 μm, parallel to ±5 μm over a lateral distance of 2 cm) where the top plate is driven at 0.05–10 μm/s by a mechanical actuator with magnetic encoder. We denote the velocity, vorticity and velocity gradient direction by x, y, and z, respectively, as shown in Fig. 2. The maximum relative plate translation along x is $L_s \sim 1$ cm, so that steady shear can be applied up to a total accumulated strain $\Delta\gamma = L_s/Z_{gap} \gtrsim 1000\%$. The cell can be operated either with the bottom plate fixed or with the plates counter propagating via an adjustable lever system, which allows the height of the zero velocity plane to be set at any distance from the bottom plate. A drop of suspension (covering an area of ~200 mm^2) is confined between the plates by surface tension. A solvent bath surrounding the plates minimizes evaporation. Wall slip, prominent in glassy systems [76], and wall-induced ordering were prevented by sintering a concentrated, disordered layer of particles – obtained by spincoating a suspension with volume fraction $\phi \sim 30\%$ – onto the glass surfaces, Fig. 3(a). We typically image a 30 μm × 30 μm × 15 μm volume in the drop (with ~3000 particles), up to ~40 μm above the coverslide.

3.4. Capillary flow

We have also studied the flow of concentrated colloidal suspensions in glass micro-channels [15,77]. Fig. 4(a) shows a sketch of a sample cell for such experiments. It is assembled by gluing a glass capillary onto a microscope coverslide with UV curing glue (Norland Optical Adhesive) by exposing it to UV light for a few minutes. Once the glass channel is attached, a glass vial (1.5 cm diameter), the bottom of which is removed, is glued on top of one end of the channel also

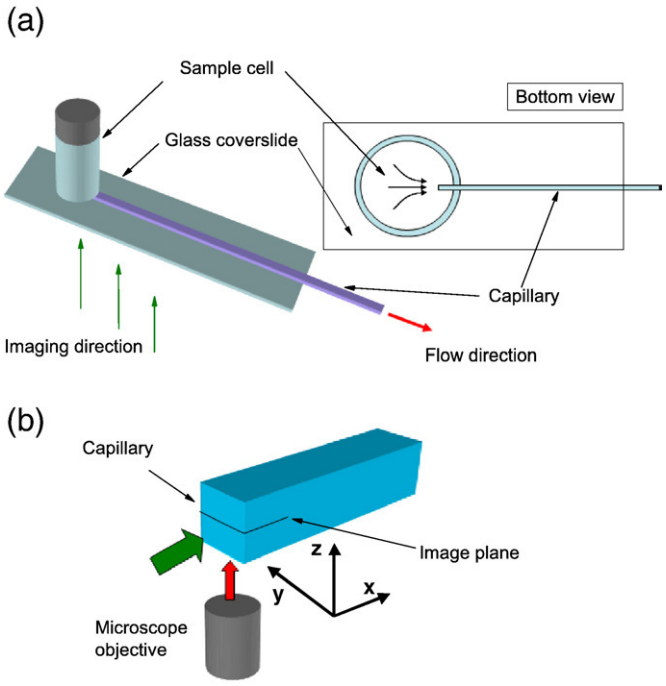

Fig. 4. (a) Sketch of the sample cell for capillary flow. The capillary is not drawn to scale. The construction is placed on the microscope stage plate and the flow is imaged from below. (b) Close up. Only the capillary and objective are drawn. The flow (green arrow) is imaged from below and 2D xy slices are collected at a depth z. (For interpretation of the references to color in this figure legend, the reader is referred to the web version of this article.)

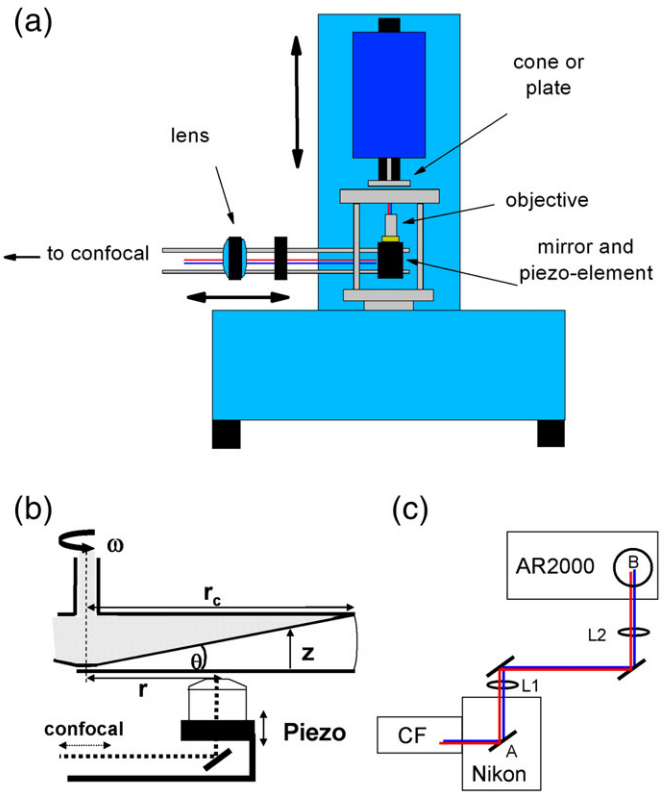

Fig. 5. (a) Schematics of the confocal rheoscope. The top arrow marks translation of the rheometer head to adjust the geometry gap, the horizontal arrow indicates translation of the arm supporting the objective to image at different radial positions. (b) Close up of the central part of the confocal rheoscope. The position of the mirror, directly underneath the piezo, is indicated as B in the right figure. (c) Global sketch of our implementation. The optical path (colored) from the confocal (CF) is guided from the back of the microscope (Nikon) via mirrors and two lenses $L1$ and $L2$, to position B corresponding to the mirror in (a). The distance between lenses $L1$ and $L2$ is $2f+d$, with f the focal length and $|d| < 0.5$ cm a small displacement to allow for lateral positioning of the objective underneath the plate. The distance between the standard position of the objective back aperture (above A) and the new one (above B) is therefore $4f+d$. (For interpretation of the references to color in this figure legend, the reader is referred to the web version of this article.)

with UV glue (2 hours exposure). Finally a PVC tube (1 mm internal diameter) is connected to the free end of the capillary and the connection is sealed with epoxy glue. The sample cell is positioned onto the microscope stage with the cover slide, forming the bottom of the cell, in direct contact with the microscope objective via the immersion oil.

All channels are borosilicate glass capillaries (Vitrocom) with rectangular (20 × 200 μm^2, 30 × 300 μm^2, 40 × 400 μm^2) or square cross sections (50 × 50 μm^2, 80 × 80 μm^2, 100 × 100 μm^2) and a length of 10 cm. The capillaries can either be used untreated, i.e. smooth on the particle scale, or have their inner walls coated with a sintered disordered layer of PMMA particles to ensure rough boundaries (Fig. 3(b)). This is achieved by filling the capillary with a 15–20% suspension of similar particles and subsequent drying in a vacuum oven at 110–120 °C.

The imaging geometry is sketched in Fig. 4(b). The flow is along the channel in the x direction; by adjusting the image size we can capture the entire cross section of the capillary. Using a modified microscope stage plate with a long rectangular slot instead of the standard circular aperture, the imaging can be performed at different positions along the channel, over a range of ≳5 cm. The suspension is first loaded into the sample cell and then driven along the channel by a constant pressure difference achieved by displacing a syringe plunger connected to the PVC tubing. During imaging, the pressure is monitored with a pressure gauge (MKS Series 902 Piezo Transducer).

3.5. Confocal rheoscope

In order to perform confocal imaging of the flow and simultaneously obtain the global suspension rheology, we have combined the fast confocal scanner with a stress-controlled rheometer (AR2000, TA Instruments), Fig. 5(a),(b). The rheometer has a custom-built, open base construction, mounted on its normal force sensor, with pillars providing space for a mirror and objective mounted on a piezo-element, which makes it possible to vary the depth of the focal plane. An aluminium plate with imaging slit is mounted on the pillars, and can be accurately levelled via three adjustment screws. A glass slide (radius 2.5 cm, thickness ~180 μm), mounted on the plate, forms the bottom surface of the measurement geometry through which the imaging is performed. The rheometer can thus be operated in plate–plate or cone plate geometry, but generally we used a stainless steel cone of radius r_c=20 mm and cone angle θ=1°. Both the glass slide and the cone can be made rough on the particle scale using the spincoating and sintering method. Evaporation can be minimized by a solvent trap, but we found superior reproducibility of the rheology of the most concentrated suspensions by slightly under-loading the geometry and applying a small rim of immiscible liquid (glycerol) around the geometry edge. Through the imaging window we can directly measure the width of the rim (typically ~1 mm) as well as the geometry area covered by the suspension. The contribution of the glycerol to the overall stress can thus be calculated; e.g. at a shear rate of 10 s^{-1} it is ~2 mPa, negligible compared to the stress levels of our suspensions, see Fig. 20. Furthermore, careful loading ensures that there is no direct contact between the sample and the glycerol rim, avoiding contamination and spurious effects due to a possible interface. Finally, we checked that bending of the cover slide was negligible, see Section 6.3.

The confocal scanner is coupled to the optics under the plate. In our setup, the scanner remains fixed in the standard configuration, connected via a C-mount to the Nikon microscope, see Fig. 5(c). To provide the coupling, we altered the optical path of the laser and the excited light. By positioning a movable mirror, the beam exits through the rear of the microscope (Fig. 5(c)) and then passes through additional mirrors and two lenses (acromat lenses, broadband coated, focal length f=18 cm, diameter=40 mm); one of the lenses is mounted on a mechanical arm, at the end of which, situated below the transparent plate, a final mirror and the piezo objective mount are located. The two lenses provide one-to-one imaging of the back aperture of the objective in its standard position on the nosepiece of the Nikon, onto that of the objective in its new position under the transparent rheometer plate. During imaging, the piezo-element is controlled by the software of the confocal microscope, providing the same 3D imaging capability as in normal operation.

4. Particle location and its limitations

4.1. Locating and identifying the particles

The first step to obtain quantitative information on particle dynamics from the images is to locate the particles. The most widely used algorithm for this purpose to date in colloid science is that of Crocker and Grier (CG) [20], with relevant software in the public domain [78].

Three main assumptions are needed in order to locate and identify the particles. The features must appear as bright objects onto a dark background, we assume that they are spherical in shape[2], and that the maximum in the brightness of a feature corresponds to its center. The concepts at the basis of feature location are still applicable to objects which do not follow these requirements but the practical algorithm for locating them will be different and generally more complicated, see e.g. [79].

Since the particle centers are identified in terms of their intensity, undesired intensity modulations which can give rise to mistakes in particle location need to be eliminated. This is achieved via image filtering using a spatial bandpass filter. This eliminates any long wavelength contrast gradients and also short wavelength pixel to pixel noise.

The coordinates of the centers of the features are initially obtained by locating the local intensity maxima in the filtered images. A pixel corresponds to a particle center if no other pixel has a higher intensity within a given distance to it; typically this distance is slightly larger than the average particle radius. These coordinates are then refined to get the positions of the particle centers with a higher accuracy by applying a *centroiding* algorithm which locates the brightness-weighted center of mass (centroid) of the particles. With this refinement procedure the coordinates of the particle centers can be obtained with sub-pixel resolution down to less than 1/10 of the pixel size [20]. The centroiding procedure proves itself effective but has some limitations. Correctly locating the particles becomes more difficult as the system becomes more concentrated and individual particle images may start to overlap. This difficulty can be dealt with by fluorescent labelling only the particle cores [33] so that images are well separated even at the highest densities. When such particles are not available, improvements in coordinate refinement may be required. Such an improvement, based on fitting the intensity profile of the particle to the 'sphere spread function' (SSF), has been devised by Jenkins [80]. We have used this method successfully for our 3D images described in Section 2. Finally, to avoid edge effects, particle centers identified within a radius from the image edge are ignored.

As noted above, the coordinates of particle centers are often found to an accuracy tied to the pixel size. This correctly implies that modifying the microscope optics so that the size of a pixel is smaller will improve the location of particle centers. In general, if the image of a particle is N pixels across, the center of that particle can be found to an accuracy of (pixel size)/N. It is important to recognize that this accuracy is different from, and often better than, the optical resolution of the microscope. The optical resolution relates to telling the difference between two closely positioned bright objects: if they are closer together than the resolution, then their diffraction-limited images blur together in the image. The resolution limit for an optical microscope is given by the wavelength of light used and the numerical aperture (NA) of the objective lens, as $\lambda/(2\mathrm{NA})$, and the best resolution for an optical microscope is about 0.2 μm. This figure reflects the wave nature of light. The accuracy with which particle centers can be located is set by different physical constraints, e.g. the fact that particles cannot physically overlap (although their images may) [20], and the knowledge that they are spherical.

4.2. Limitations

The above mentioned accuracy of locating particles is intrinsic, and applies even for particles frozen in the image. It can be estimated from the plateau value of the mean squared frame to frame displacements (which we denote as MSFD) measured in a close packed sediment, where particles are essentially immobile. In general however, additional errors on the exact center position arise from short time diffusive motion and flow advection during acquisition of the particle image, if the images are from a scanning system (such as a confocal microscope) which does not acquire each pixel simultaneously.

Let us estimate these effects for 2D and 3D imaging. For the 2D case, given the frame acquisition rate f_{scan} and the image size in pixels

[2] In actual fact, due to a possible different pixel size in the x, y and z directions the images may not appear as spherical; the crucial assumption is that the imaged features are *spherical in reality*. Any stretching of the image can then be removed prior to the location procedure.

$(n\times m)$, the time required to scan one line is $\simeq 1/(nf_{\mathrm{scan}})$. If $\tilde{a}$ is the particle radius in pixels, then the time required to image a particle is:

$$t_{\mathrm{im}}^{2D} = 2\,\tilde{a}/(nf_{\mathrm{scan}}). \quad (1)$$

With our imaging system, a 256×256 pixel image can be taken at $f_{\mathrm{scan}}=90$ Hz. Using a 100× magnification objective, for which the xy pixel size is ~0.2 μm, the time to acquire a 2D image of a particle with radius $a=1$ μm is therefore $t_{\mathrm{im}}^{2D}\simeq 0.4$ ms.

For 3D images, acquired as a z-stack of 2D slices, the limiting factor is the speed at which the particle is imaged in the z-direction. The voxel size in the z direction (i.e. the z-spacing between the 2D slices) may differ from that in the x and y direction. Denoting the particle radius in z-pixels by $\tilde{a}_z$, the time required for a 3D particle image is:

$$t_{\mathrm{im}}^{3D} = 2\,\tilde{a}_z/f_{\mathrm{scan}}, \quad (2)$$

with f_{scan} the acquisition rate for a complete 2D image as before. Thus, for the 3D case, using again $f_{\mathrm{scan}}=90$ Hz and a typical value of 0.2 μm for the z-pixel size, the acquisition time for our $a=1$ μm particle is $t_{\mathrm{im}}^{3D}\simeq 0.1$ s.

We first consider the (short time) diffusive motion of colloids in a suspension on these time scales. In the dilute limit, the diffusion constant is $D_{s,0}=(k_BT)/(6\pi\eta a)$, with k_B the Boltzmann constant and η the solvent viscosity. For concentrated suspensions the short time diffusion constant is reduced due to hydrodynamic hindering, $D_s(\phi)=D_{s,0}H(\phi)$ with $H(\phi)<1$ [81–85]. The average motion in one direction during the acquisition time is $\sqrt{2D_s(\phi)t_{\mathrm{im}}}$, i.e. the additional error is $\delta=\sqrt{2D_s(\phi)t_{\mathrm{im}}/2}$. Using $\eta=2.7\times10^{-3}$ Pa·s for our solvent (decalin) and $T=300$ K, $D_{s,0}=8.13\times10^{-2}$ μm^2 for the $a=1$ μm colloid. The resulting error due to thermal displacement during 2D imaging of a dilute system is then $\delta_{2D}\simeq 2$ nm, while for the 3D case, using the same frame rate and z-pixel size as above, we have $\delta_{3D}\simeq 35$ nm. While the former is considerably smaller than the intrinsic 1/10 pixel accuracy (~20 nm), for 3D the thermal motion is the limiting factor. Note that these considerations apply to hard sphere systems only; when additional interactions limit the short time displacements, the intrinsic 1/10 pixel limit may still apply.

Flow can also induce additional errors on the particle location due to image distortion. Since the image of a particle is scanned either via lines in 2D or via horizontal slices in 3D, it will be distorted because the particle is displaced between two consecutive lines as well as slices. Such distortion can be exploited to deduce the local flow velocity, see [68], but here we are interested in the velocity range for which the distortion is sufficiently small to consider the object as effectively spherical. The particle speed beyond which this no longer holds can be estimated by comparing the imaging time t_{im} with the time t_f required for the flow to displace the particle over its own diameter. For a flow velocity $\tilde{V}$ (in pixels per second), $t_f=2\tilde{a}/\tilde{V}$. We consider the particle significantly distorted if $t_{\mathrm{im}}/t_f\geq 0.1$, i.e. a distortion of 1 pixel for a particle size $2\tilde{a}=10$. Using Eqs. (1) and (2) for the acquisition times, the maximum velocities are:

$$\tilde{V}_{2D}^{max} = 0.1nf_{\mathrm{scan}}, \quad \tilde{V}_{3D}^{max} = 0.1f\,\tilde{a}/\tilde{a}_z. \quad (3)$$

For typical parameters ($f_{\mathrm{scan}}=90$ Hz, $n=256$ pixels, 1 pixel ≃ 0.2 μm) the limiting velocity in 2D is $V^{max}\sim 500$ μm/s, while for 3D images we obtain $V^{max}\sim 2$ μm/s for an x to z pixel size ratio of 1:1. In both cases, further improvement could be achieved by removing the distortion prior to locating the particles via image correlation procedures [68]. In principle, improvement could also be achieved by using a location algorithm with a particle template or Sphere Spread Function [80] with a distorted shape, but since this requires a priori knowledge of the flow field, the removal of distortion prior to particle location is more practical.

5. Tracking algorithms

Once the coordinates have been found in each frame, they need to be merged into trajectories describing the particle motion. In this 'tracking' procedure, each particle is labelled with an identification tag and an algorithm looks for particles in the following frame that can be assigned the same tag. Tracking has applications in fields as diverse as robotics and biophysics [79,86,87]. In the field of digital image processing a variety of methods has been devised [88]. In each method, a specific cost function is calculated based on the changes in coordinates for each set of identifications, possibly extended with a cost function for change in feature appearance [88]. The 'correct' identification is then obtained as the one for which the cost function is minimized.

5.1. The classic CG algorithm

5.1.1. Tracking algorithm

The algorithm we use, devised by Crocker and Grier (CG), is based on the dynamic properties of non-interacting colloids [20]. The cost function in this case is the mean squared frame to frame displacement (MSFD, as defined before) of particles between frames. Given the position of a particle in a frame and all the possible new positions, in the following frame, within a tracking range R_T of the old position, the algorithm chooses the identification which results in the minimum MSFD. Particles moving farther than R_T between frames are unable to be tracked, and are either mis-identified as other particles, or else treated by the algorithm as new particles.

Note that the original CG algorithm also includes the ideas discussed in Section 4; here we focus on tracking particles between successive frames, rather than locating particles in a single image. These two parts of the CG algorithm are decoupled: the tracking method works independently of how the particles were originally identified.

5.1.2. Hard particle simulations

Crocker and Grier tested their algorithm by tracking the self-diffusion of particles in dilute colloidal suspensions [20]. Since then, the algorithm has been applied in various studies of quiescent colloidal systems [19,31]. However, quantitative studies of its tracking performance in realistic concentrated systems, possibly with additional motion on top of Brownian diffusion, have not been performed to date. In fact, the study of concentrated systems explicitly pushes the CG tracking algorithm beyond its design parameters. We therefore apply the classic CG algorithm to computer generated data, in which the particle identity is known *a priori*, and evaluate its performance for quiescent systems of different densities and for various imposed particle motions. Quiescent data were generated by Monte-Carlo (MC) simulation of hard-disks in two dimensions and of hard-spheres in 3D (see e.g. [89]) imposing mean squared displacements between each MC iteration chosen to obtain a sufficient success rate. We simulated $N>1200$ particles and, as in experimental data, particles may (dis) appear at arbitrary times around the edge of our simulation cell.[3]

We take the data from the simulations, and treat it as the raw data of particle positions for the classic CG-algorithm. Specifically, we use the CG-algorithm to track particles between MC-iterations i and $i+n$, for which the *true* MSFD is $\langle\sum_j(r_i^{j}{}_{+n}-r_i^j)^2\rangle=\langle\Delta r_n^2\rangle$, with $j=x, y, z$. The key idea of the CG-algorithm is that ideally, between each frame of the movie, the majority of particles should move less than the typical interparticle (center-to-center) spacing ℓ. In other words, it is desirable for the MSFD to be less than ℓ^2. In fact, since the MSFD is

[3] Similar to Ref. [89], we observe, at sufficiently high concentration, a transition from short ('in-cage') to long-time ('cage breaking') diffusion in the mean squared displacement $\langle\Delta r^2(\Delta t)\rangle$ (the 'MSD'). In addition, in 2D, our hard-disk system shows dislocation mediated, two stage, melting according to the Kosterlitz-Thouless scenario, with a melting density $\phi_{2D}\sim 0.7$, see [90]. For 3D our densities are also below the freezing fraction $\phi_{3D}^F=0.494$. Our simulations are by no means exhaustive, they are merely performed to test the success of the tracking algorithm.

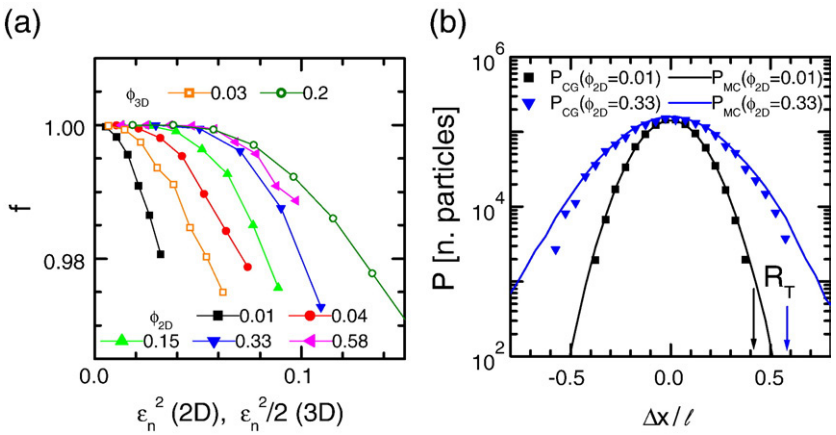

Fig. 6. (a) The fraction of correctly-tracked particles, f, versus the normalized true MSD ϵ_n^2 between tracked frames for MC simulations of hard-disk fluids at various densities ϕ_{2D} and 3D hard-sphere fluids at ϕ_{3D}=0.03 and ϕ_{3D}=0.2. Note the different x-axis for the 2D and the 3D case. (b) Corresponding distribution of normalized displacements $P(\Delta x/\ell)$ for two densities ϕ_{2D}, taken for $f\simeq 0.98$. Solid lines: the true PDF over n MC steps. Symbols: P_{CG} as obtained from classic CG tracking between frame i and $i+n$, for ϕ=0.01 (■) and ϕ=0.33 (▼).

calculated by averaging over *all* particles, many particles will have larger motions; likewise ℓ is an average over all particles, so that some particles are closer together. Thus, in practice, it is desirable that the MSFD is much less than ℓ^2.

To quantify this last statement, we tracked simulated particles between frames with progressively larger normalized MSFD, $\epsilon_n^2 \equiv \langle \Delta r_n^2 \rangle / \ell^2$, by increasing n, and tested how the CG-algorithm performed when pushed past its original design parameters. For each ϵ_n^2, we measured the fraction f of correctly tracked particles. We checked in all cases that the vast majority of the tracking errors are generated in the bulk of the system rather than at the boundaries.[4]

5.1.3. Quiescent system

In Fig. 6(a) we show f as function of ϵ_n^2 for the 2D system at different ϕ_{2D} and ϕ_{3D}. As expected, f decreases with increasing ϵ_n, but the performance in more concentrated systems is considerably better than in the dilute case. To quantify this, we impose a criterion for 'successful tracking' of $f>0.99$, and we find that the algorithm works up to ϵ_n=0.15 at the lowest ϕ_{2D} studied, but this figure rises and essentially saturates at ϵ_n=0.3 at the highest ϕ_{2D}. This behavior reflects the difference in structure between a dilute and concentrated system. While ℓ is the average nearest neighbor spacing, in a dilute system, particles can approach much closer than this (although still limited to be at least $2a$ apart). In this case, two closely spaced particles could potentially swap positions and confuse the tracking algorithm. In contrast, for a concentrated system, $\ell \approx 2a$, and it is much harder for particles to swap positions. Thus in a concentrated system there are fewer misidentifications for a given value of ϵ compared to a dilute system with the same ϵ. For the 3D systems, the performance at large concentration is even better, i.e. for ϕ_{3D}=0.2, the algorithm works up to $\epsilon_n \simeq 0.4$.

An experimental diagnostic for correct tracking is the distribution of particle displacements from frame to frame, $P(\Delta x)$[5]. For correct tracking it should vanish smoothly within the tracking range. Fig. 6(b) compares the true distribution function over n frames, P_{MC}, with that resulting from the classic CG tracking between frames i and $i+n$, P_{CG}, for two densities and n such that $f\simeq 0.98$. In both cases P_{CG} follows the simulation data for $\Delta x < R_T$, beyond which is cut-off, and the discrepancies with P_{MC}, due to the misidentified particles ($1-f$=2%), appear in the large $\Delta x/\ell$ tails (clearer in the denser case). Note that the CG algorithm is able to follow particles for larger tracking ranges in the case of larger area (or volume) fractions.

5.1.4. 2D system in shear flow

To test the performance of classic CG tracking in the presence of non-uniform motion, we superimpose affine shear and random displacements with a MSFD of $(\epsilon\ell)^2$ on a single 2D MC configuration with ϕ_{2D}=0.33. The strain increment between frames is $\Delta\gamma$, i.e. the affine x-displacement over one frame for particle k is $\Delta\gamma(y_k-\bar{y})$ (subtracting $\bar{y}$ guarantees zero net motion), again with periodic boundary conditions. We analyze data only over accumulated strains <20%, so that shear does not bring neighboring particles in close proximity, avoiding 'artificial' reduction in performance (see Section 5.3.2 and Fig. 12). The true origin for tracking errors is the increase in the *difference* in advected displacements between different parts of the image, the maximum of which is $\Delta S_x/\ell = L_y\Delta\gamma/2\ell$ in units of the average spacing, with L_y the system size in the velocity gradient direction. Fig. 7(a) shows that f rapidly decreases for $\Delta S_x/\ell \gtrsim 0.4$.

From the resulting tracks, we obtain the distribution of non-affine frame to frame displacements after subtracting the affine shear as evaluated from the classic CG trajectories. The results for x and y displacements are shown in Fig. 7(b). For $\Delta S_x/\ell$=0.25 the result is identical to that without shear, matching the superimposed random motion. For $\Delta S_x/\ell$=0.54, the distribution of y-displacements appears very close to the correct distribution, but the deformed central peak of P^x and the presence of prominent side bands show that tracks have been evaluated incorrectly. The reason for the side bands to appear is linked to the fact that, for large shear, the algorithm ends up picking the wrong comoving frame, due to the fact that a large fraction of particles are misidentified.

5.1.5. Summary of evaluation of CG tracking

We have shown that the classic CG algorithm can track particles between consecutive frames for a maximum MSFD $(0.3\ell)^2$ in quiescent concentrated hard-sphere-like systems, but considerably less in dilute systems. These limits are similar to those discussed in the original article by CG [20]. Simply put, for larger displacements, the problem of uniquely identifying particles becomes ill-posed, as the possibilities of particles exchanging places become too significant. No algorithm can succeed in this case, and the only remedy is to acquire images at a faster rate to resolve the intermediate steps.

Further, for non-uniform flow the limit is set by a maximum *difference* in advected motion of ~0.4ℓ over the full image. We also found that cut-off and distortion effects in the distribution of particle displacements can indeed be used as diagnostic of incorrect tracking,

[4] We note the following points: (1) The particle radius a is not relevant to the tracking algorithm, and matters in the simulation only as a hard-particle constraint and determines the density of the system via the area or volume fraction, ϕ_{2D} or ϕ_{3D}, respectively. (2) The tracking range R_T used to test the CG-algorithm is the largest possible beyond which combinatorics become excessive.

[5] This is also known as the self-part of the van Hove correlation function.

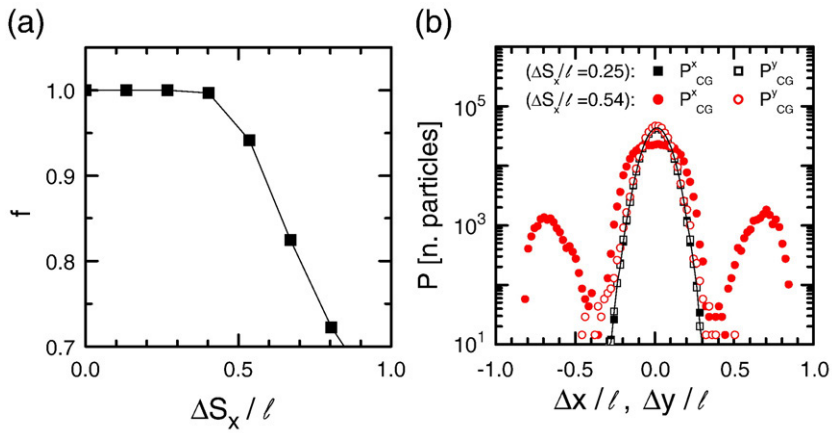

Fig. 7. Evaluation of classic CG tracking under shear: (a) f versus the normalized maximum difference in advected displacement between frames $\Delta S_x/\ell = L_y\Delta\gamma/2\ell$ for $\phi_{2D}=0.33$ and $\epsilon^2=0.005$. (b) The distribution of normalized displacements $P(\Delta x/\ell)$ and $P(\Delta y/\ell)$ for $\Delta S_x/\ell=0.25$ (squares) and $\Delta S_x/\ell=0.54$ (circles). Solid line: result without shear.

although one should be cautious to interpret the absence of such features as proof of 100% performance. The next subsection discusses a simple modification of the classic CG algorithm to deal better with particles in uniform or non-uniform flow.

5.2. Iterated CG tracking algorithm

5.2.1. Description

The classic CG algorithm was designed for cases where all particles move randomly (due to Brownian motion). However, many interesting cases have particles moving in a flow with larger coherent structures, perhaps also with Brownian motion superimposed, or even simply noise. For example, the coherent motion could be due to Poiseuille flow through a pipe, overall drift of the field of view, or an induced shear flow. If the magnitude of this motion is small, the classic CG algorithm still has some ability to track particles. Following the logic above, tracking should work reasonably well if the distance most particles move between frames is moderately less than the inter-particle spacing ℓ, whatever the origin of this motion may be.

In cases where the motion is simple and small compared to ℓ, the classic CG algorithm can be iterated to produce better results. This "Iterated Tracking" method is as follows. (i) First identify the particle positions at each time, as per Section 4. (ii) Track the particles using the classic CG algorithm. (iii) Determine the coherent motion from the successfully tracked particles. (iv) Remove the coherent motion from the original particle positions. (v) Repeat steps ii–iv until most particles are successfully tracked, and the residual coherent motion detected in step iii is reduced to an acceptable level. (vi) Add back in all of the coherent motion that has been previously subtracted in all iterations of step iv.

As long as the motion of most particles is less than the tracking limit R_T and thus less than the interparticle spacing ℓ, at least a few particles will be successfully tracked in the first iteration. The coherent motion of these few particles is then used to 'bootstrap' the classic CG algorithm, and in the subsequent iterations, more particles are correctly tracked. These then refine the coherent motion and thus the Iterated Tracking method eventually is able to converge on the correct trajectories for all the particles. In practice, this usually only takes 3–4 iterations to produce good results. The key to iterated tracking is that the first tracking step must *correctly* track enough particles to start the process. We use our simulated data to study the breakdown of Iterated Tracking in a test case.

5.2.2. Uniformly moving system

We first superimpose a uniform x-displacement s_n over n MC steps on top of the MC dynamics. Periodic boundary conditions keep particles within the analysis window. We then perform Iterated Tracking on these particle positions. Fig. 8(a) shows f versus s_n for two densities ($f(s_n=0)>0.995$ in both cases). For small s_n, $f\simeq f(s_n=0)\approx 1$, but for $s_n/\ell \gtrsim 0.5$ very few correct tracks are found. Note that Iterated Tracking still provides a result, but mostly consisting of incorrect tracks, and yields incorrect motion; in this case, the first tracking step

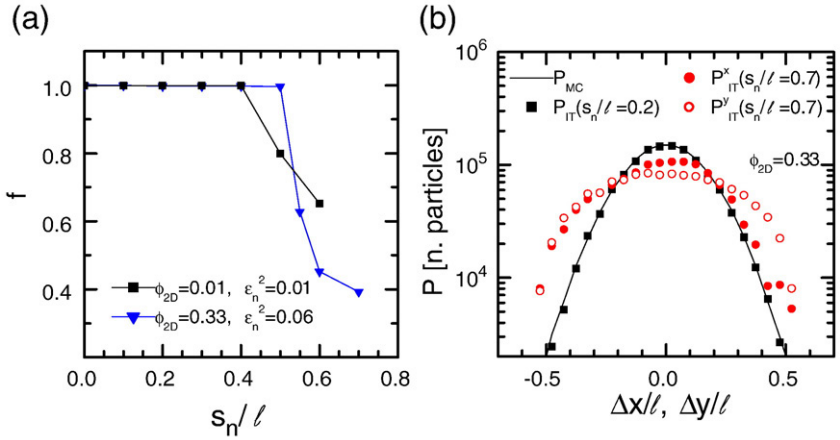

Fig. 8. Iterated tracking results. (a) f versus the normalized shift s_n/ℓ between frames for $\phi=0.01$, $\epsilon_n^2=0.01$ and $\phi=0.33$, $\epsilon_n^2=0.06$. (b) PDF's in the co-moving frame for $\phi_{2D}=0.33$ and two 'drift' velocities: Line: the true PDF over n MC frames. (■): P_{CG} for $s_n/\ell=0.2$, (●): distribution function of x-displacements P^x_{CG}, in the co-moving frame for $s_n/\ell=0.7$, (○) same for y-displacements.

has failed and subsequent tracking steps are unable to improve the results. In Fig. 8(b) we show the distribution of particle displacements in the *co-moving frame* for two values of s_n/ℓ. By construction, the true P_{MC} is identical to that in the quiescent system, while P_{IT} is the displacement distribution in the co-moving frame, i.e. the frame where the average displacement of the 'IT-tracks' (obtained via the Iterated Tracking algorithm) vanishes. The breakdown of iterated tracking for $s_n/\ell=0.7$ in the $\phi=0.33$ system is brought out by the sharp cut-off of $P(\Delta x>R_T)$, and, more prominently, by the asymmetry in the distribution of displacements P_{IT}^{x} along the direction of motion.

The results are similar for non-uniform flow. If the maximum motion in any area of the data exceeds ~0.4ℓ, that region will be poorly tracked. For example, with the shearing data discussed in Section 5.1.4, at each iteration step the measured shear strain can be removed, but this method will still have difficulties when $\Delta S_x \gtrsim 0.4$. With care, trajectories found in regions with motion less than 0.4ℓ may be used to extrapolate the motion to the more mobile regions. Note that the classic CG algorithm was not intended for tracking particles in flow, so that the success of Iterated Tracking in non-trivial cases reveals the strength of that algorithm.

5.3. Correlated image tracking

5.3.1. Description

Due to the limitations shown above, 2D or 3D images with large drift or non-uniform motion require a modified analysis for correct tracking. Similar shortcomings of standard tracking for granular flows have been discussed in [71] and analysis of such data will also benefit from the correction method we describe in this section. The basic ingredients of "Correlated Image Tracking" are: (i) We first obtain the particle coordinates as explained in Section 4. (ii) We then obtain independent information on the advected motion and its spatial and time dependence via PIV-type correlation analysis of the raw images. (iii) Next, this (time and position dependent) advected motion is subtracted from the bare particle coordinates. This yields the particle coordinates in a 'locally co-moving' ('CM') frame. (iv) In the CM frame, the particles can be tracked as in a quiescent system. The tracking efficiency is essentially limited by the value of the MSFD or non-affine motion in the CM frame. (v) After tracking, the advected motion is added back to the particle coordinates to obtain the trajectories in the laboratory frame.

To identify frame to frame advective motion, we use standard PIV-type image correlation methods [41]. Consider a region of size $n\times m$ pixels of two consecutive 2D images $i-1$ and i. Let $I_{i-1}(x, y)$ and $I_i(x, y)$ be the intensity patterns as function of position (x, y) of these (sections of) images. The covariance is defined as:

$$cov[I_{i-1}(x,y), I_i(x,y)] = \frac{1}{[(n\times m)-1]} \sum_{p=1}^{n} \sum_{q=1}^{m} \left[I_{i-1}^{pq} - \langle I_{i-1}\rangle\right]\left[I_i^{pq} - \langle I_i\rangle\right], \tag{4}$$

where I_{i-1}^{pq} and I_i^{pq} are the intensities of the pixel corresponding to position (X_p, Y_q) in each image and $\langle I_{i-1}\rangle$, $\langle I_i\rangle$ are the respective average intensities defined as $\langle I\rangle = \frac{1}{[n\times m]} \sum_{p=1}^{n} \sum_{q=1}^{m} I^{pq}$. Analogously, the variance of a single image I is:

$$var[I(x,y)] = \frac{1}{[(n\times m)-1]} \sum_{i=i}^{1} \sum_{j=1}^{m} \left(I^{ij} - \langle I\rangle\right)^2. \tag{5}$$

The correlation coefficient $c[I_{i-1}(x,y),I_i(x,y)]$ of the two images is defined as:

$$c[I_{i-1}(x,y), I_i(x,y)] = \frac{cov[I_{i-1}(x,y) I_i(x,y)]}{\sqrt{var[I_{i-1}(x,y)] var[I_i(x,y)]}}. \tag{6}$$

The motion is obtained by shifting image i by a certain number of pixels $(\Delta X', \Delta Y')$ and computing the correlation coefficient $c[I_{i-1}(x,y), I_i(x-\Delta X', y-\Delta Y')]$. This is repeated for shifts within a desired range until c is maximized for $\Delta X'=\Delta X$, $\Delta Y'=\Delta Y$. Repeating the procedure over subsequent frames yields the displacement as function of time $(\Delta X, \Delta Y)(t_i)$ in the region of the image series under consideration, Fig. 9. For strongly time-dependent flows, a scan over all possible $\Delta X'$, $\Delta Y'$ in this region is required, but for smooth flows we have implemented a more efficient method in which image i is scanned in a narrow range centered around the shift $(\Delta X, \Delta Y)(t_{i-1})$ found from the previous images. A key point to recognize is that these shifts are quantized by the size of a pixel, so while the motion obtained from image correlation is a good starting point for the tracking, the subsequent tracking is necessary to achieve subpixel resolution of particle motion.

In most applications one can identify, at least within the microscope field of view (see Section 3.5), a principal axis along which the flow takes place. The entire image can then be rotated such that the advective motion occurs in only one direction, which we denote by x. To obtain the advection profile over the entire image, the correlation method is applied in different ways depending on the uniformity of the motion and image dimensionality, as we describe now.

For 2D images, when the motion is spatially uniform in the xy plane, the above procedure is applied to the entire image, Fig. 10(a), resulting in $\Delta\mathbf{R}(\mathbf{r},t_i)=\Delta X(\mathbf{r},t_i)=\Delta X(t_i)$. The advective motion can also depend on the position y transverse to the flow, see Fig. 10(b). The image is then decomposed into strips, which are shifted and correlated separately, yielding an advection profile $\Delta X(y_q)$ discretized at the centers y_q of the strips.

For 3D images, the basic manifestation of nonuniform flow is simple shear, Fig. 10(c), where the average motion is a function of z only. The sheared volume is then decomposed in xy slices at different z and the correlation procedure is performed on each 2D slice separately. A more complex flow is shown in Fig. 10(d), where shear occurs both in the y and z direction, as for instance in 3D channel flows. Here the 3D images are first decomposed in xy slices at different z and then each slice is further decomposed in y-bins for which the motion is analyzed.

In the most general form $\Delta\mathbf{R}$ is both position and time dependent, $\Delta\mathbf{R}=\Delta\mathbf{R}(\mathbf{r},t_i)$, and includes shifts in all three directions $\Delta X(\mathbf{r},t_i)$, $\Delta Y(\mathbf{r},t_i)$, $\Delta Z(\mathbf{r},t_i)$. For example, in experiments where a point-like force source is applied in the medium, e.g. by dragging a magnetic or tracer bead through a colloidal suspension [91], the direction and the magnitude of the 'advected' motion depend on x, y and z. In such a case the imaged area (volume) must be decomposed into squares (cubes), and a full PIV analysis must be carried out to characterize the motion $\Delta\mathbf{R}(x_p,y_q,z_r,t_i)$ in each element p, q, r. Another example is

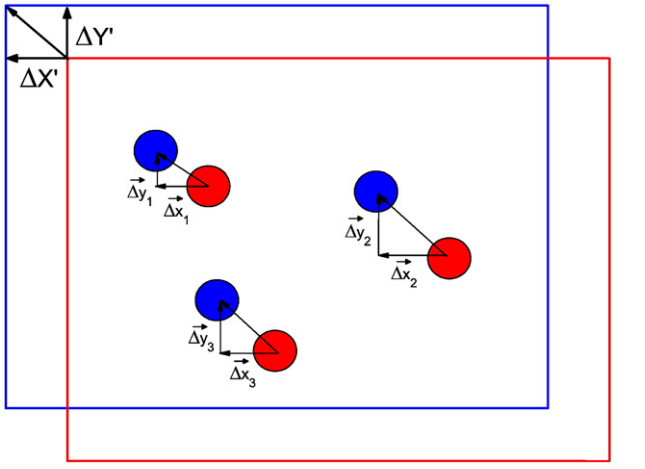

Fig. 9. Illustration of the shifting and correlation procedure. Each particle in the section of the image under consideration is displaced by $(\Delta x,\Delta y)$ between frame 1 and frame 2. The entire image section is shifted over a range of values $(\Delta X',\Delta Y')$ to find the optimum shift $(\Delta Y,\Delta Y)$ that maximizes the correlation.

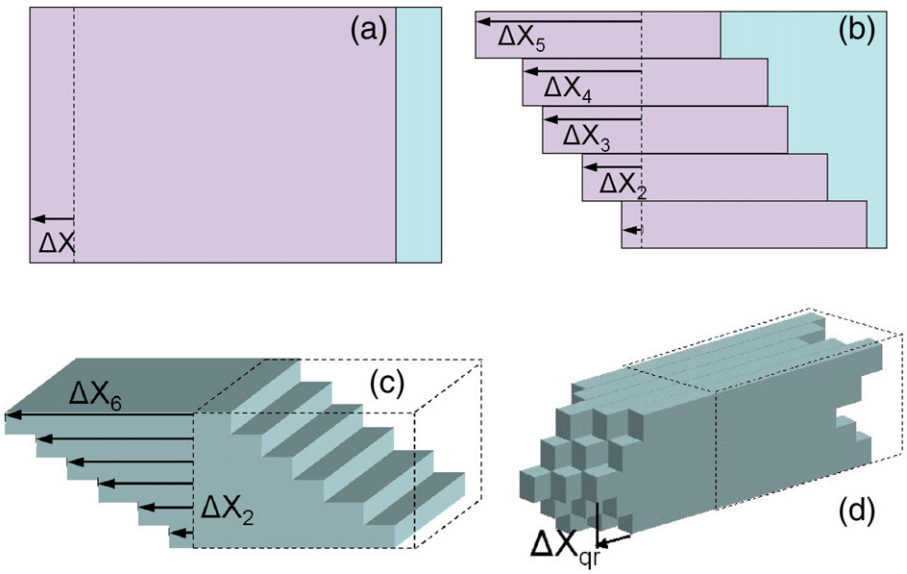

Fig. 10. Examples of 2D (a, b) and 3D (c, d) image correlation procedures. (a) A uniform shift ΔX across the entire field of view maximizes the correlation. (b) The advected motion is a function of y; the image is then decomposed in bins centered at y_q, each of which is shifted by $\Delta X(y_q)$ to obtain maximum correlation. (c) The motion is a function of z only. The 3D image is decomposed in slices centered at z_r, each of which is shifted by $\Delta X(z_r)$ to obtain maximum correlation. (d) The advected motion is a function of y and z. Decomposition into y and z bins yields the advection profile $\Delta X(y_q,z_r)$.

sedimentation, where $\Delta X=0$, $\Delta Y=0$ but ΔZ depends on z. Extensions to our algorithm dealing with such cases are possible but we have not implemented this. For our experiments (simple shear or channel flow) it suffices to consider shifts in one direction, which are independent of the coordinate in that direction.

Once the advected motion has been measured, the discrete displacement profile $\Delta\mathbf{R}$ (x_p, y_q, z_r, t_i) is then interpolated to give the continuous profile $\Delta\mathbf{R}$ (x, y, z, t_i). This is more appropriate to subtract from the particle coordinates, which are themselves continuously distributed. Using the continuous profile, the transformation of the position $\mathbf{r}_k(t_i)=[x_k,y_k,z_k](t_i)$ of particle k in the laboratory frame to its position $\bar{\mathbf{r}}_k(t_i)$ in the CM frame of reference is:

$$\bar{\mathbf{r}}_k(t_i) = \mathbf{r}_k(t_i) - \sum_{j=1}^{i} \Delta\boldsymbol{R}\left(\mathbf{r}_k(t_i), t_j\right), \tag{7}$$

where $\Delta\mathbf{R}(\mathbf{r}_k(t_i),t_j)$ is the *past* motion between frame j and $j-1$, at the *current* location $\mathbf{r}_k(t_i)$ of the particle. This reduces to $\Delta\mathbf{R}(\mathbf{r},t_j)=\Delta X(y,z,t_j)$ for our experiments.

In the CM frame, the average particle motion (nearly) vanishes. The use of the classic CG algorithm at this point therefore allows particle tracking limited only by the MSFD in the CM frame. Occasionally, the CM tracks show some residual motion, in which case a modest improvement may be obtained by using Iterated Tracking (Section 5.2). We also note that, in the event that a clearly *anisotropic* non-affine motion is found after a first CM tracking step, it could be beneficial to perform the tracking in the CM-frame again using an ellipsoidal shape of the tracking area or volume rather than the standard circular or spherical shape defined by the range R_T. However, the examples discussed in Section 6 did not require such a modification and we have not implemented this.

Once tracking is completed, the advected motion $\Delta\mathbf{R}$ is added back by inverting Eq. (7). This then provides the trajectories of the particles in the laboratory frame of reference.

5.3.2. Limitations of correlated image tracking

A possible limitation to Correlated Image Tracking is a failure of the PIV-type correlation method. This could arise when the frame to frame shifts are a significant fraction of the actual image or image-bin size. However, this method can work successfully for quite large shifts amounting to nearly the image size. To show this, we analyzed an experimental image series taken from plug flow. In this image series, the motion was slow enough that classic CG tracking worked; we use the results of this tracking as the "true" motion. Furthermore, there was little relative particle motion (nearly zero MSFD). We then took pairs of images from this image series, separated by n frames, to model an effectively much faster flow rate. From the tracking, we know the shift ΔX^{tra} that should best align these two images. For each pair of images, we calculate the shift ΔX^{shift} from image correlation, and compare that apparent shift to the true shift ΔX^{tra}, in Fig. 11 (red symbols). The correlation coefficient (thin blue line) decays roughly linearly with ΔX^{tra}, in line with the reduction of the correlated portion of the images, and plateaus at a value ~0.2, corresponding to the coefficient for two entirely different images of the same system. The latter value is specific to our high density system, and may vary for different systems.

When comparing the image at time j and the shifted image at time $j+1$, it is important to note that in each case the full image is

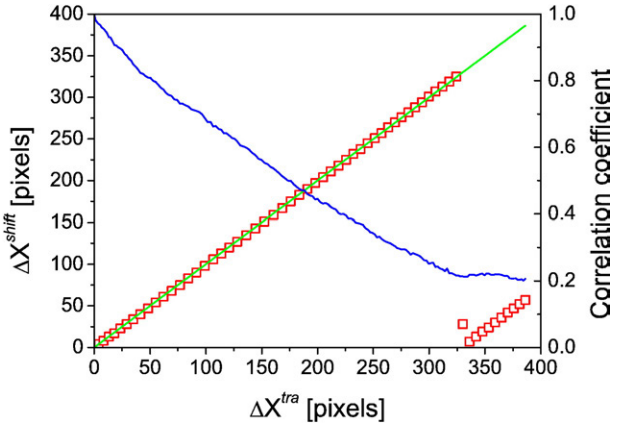

Fig. 11. Test of the shift-correlation procedure on images of plug-flow. The shift in the flow direction ΔX^{shift} (■), obtained from the correlation method, is plotted against the exact accumulated displacement obtained from tracking ΔX^{tra} (–), see the text. Image size: 331×580 pixels. Right axis: correlation coefficient (blue line) versus ΔX^{tra}. (For interpretation of the references to color in this figure legend, the reader is referred to the web version of this article.)

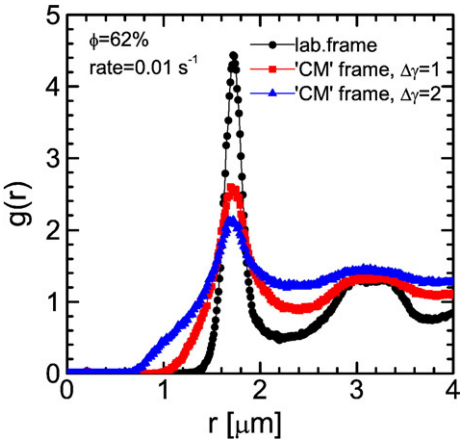

Fig. 12. Short distance behavior of the pair correlation function $g(r)$ from 3D coordinates of a sheared colloidal glass (ϕ=0.62, a=850 nm), in the laboratory frame (●), in the locally co-moving ('CM') frame after subtracting advected motion corresponding to an accumulated strain of $\Delta\gamma$=100% (■), and $\Delta\gamma$=200% (▲). The local shear rate is $\dot{\gamma}$=0.01 s^{-1}, strain accumulation during acquisition of a single 3D stack is ~1.5%, while between frames it is 4%. The data show that particles may come in close proximity after removal of large advected motion.

compared. Thus the shifted image at j+1 has some pixels wrapped around from one edge of the image to the other, which has no physical meaning. An alternate idea would be to crop the two images, so that any pixels shifted outside the boundary are removed. Thus, when considering very large shift factors approaching the width of the image, only two narrow strips of the two images would be compared to determine the correlation coefficient. We find that this method is generally less successful, despite its intuitive appeal. When the required shifts are large, generally using the full image is more likely to find the correct shift value. Comparing the large regions of the two images that could be potentially cropped, these will be uncorrelated, and thus in general the correlation coefficient is dominated by the small regions that correctly overlap. This then yields the results of Fig. 11 where the correct shift value is found even for ΔX^{tra} almost as much as the full width of the image.

A stronger limitation to the correlation procedure is an excessive amount of *relative* particle motion between frames. This obviously limits the correlation compared to that of plug flow described above, but, more directly, large relative displacements cause failure of classic CG tracking in the CM frame, as discussed in Section 5.1.3. In practice we found that a maximum MSFD in the co-moving frame (the non-affine motion) of ~$(0.3\ell)^2$ is the limiting value for the method to work.

Non-affine motion during flow has an additional effect which may limit the tracking performance when subtracting shear advection accumulated over many frames. Suppose two particles start off as nearest neighbors, at a distance ≥2a, but at streamlines with different velocities. After one frame, when the advected motion is subtracted, they remain at that distance if their motion was fully affine. In contrast, *with* non-affine motion, their separation after advection removal may become <2a, that is, they would apparently be in contact. Over single frames this effect is limited, i.e. particle separations still considerably exceed their non-affine displacements between frames and tracking is not affected. However, after multiple frames, the non-affine displacements can accumulate and the particle separation in the CM frame may have been reduced to a value comparable to the non-affine frame to frame displacements. This gives rise to tracking errors based on the same arguments as in Section 5.1.3. The artificial reduction in particle separation in the CM frame is visible in the pair correlation function $g(r)$, Fig. 12, where we see that some particles apparently overlap after the removal of large advective motion.

This problem is remedied by *piecewise tracking* of particles in intervals over which the accumulated relative motion is small. Each interval the particles are assigned their identification tag, and the full trajectory is obtained by matching the tags in a one-frame overlap of the intervals. For the case in Fig. 12, particle separations in the co-moving frame are ≥a for accumulated strains $\Delta\gamma \leq 100\%$, so that tracking is only affected for $\Delta\gamma > 100\%$, but in general a different limit may apply since non-affine motion does not necessarily scale with accumulated strain [70] and may depend on ϕ.

Summarizing, the main advantage of Correlated Image Tracking is that particles are tracked in a *locally co-moving frame of reference* where limitations to tracking are the same as in a quiescent system, as described in Section 5.1.3. In other words, our method permits the tracking of particles in flowing colloids to the same level of accuracy as that in non-flowing systems.

6. Applications

In this section, we give example results from particle tracking in the two flow geometries already introduced in Section 3, viz., simple shear and capillary flow. We also describe the application of the

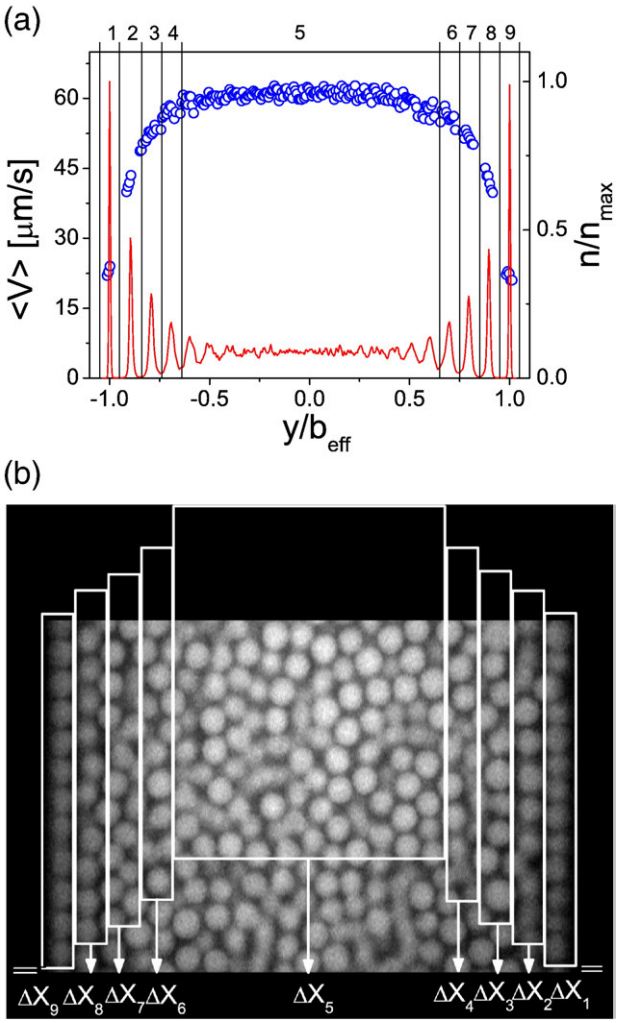

Fig. 13. (a) Velocity profile (○, left axis) and histogram of particle positions (—, right axis) as a function of the transverse coordinate y normalized by effective channel half-width $b_{eff}=b-a$. The experiment refers to the flow of a 63.5% suspension in a $2b$=50 μm wide smooth, square channel. The particles are arranged in well defined layers close to the walls and the shear decays towards the channel center where the suspension flows as a plug. The vertical lines highlight the y-bins and the numbers match those in Fig. (b). (b) Illustration of the non-uniform shifts during 2D channel flows. The resulting displacements $\Delta X(y_q)$ (q=1....9) are subtracted from the particle coordinates. Image size: 34 μm×50 μm.

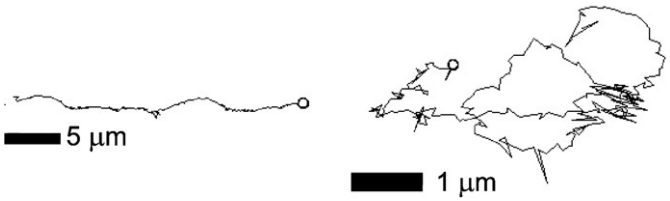

Fig. 14. Example of particle tracks in the laboratory (left) and in the co-moving frame (right). Circles indicate the start of the trajectory. The particle is situated in a shear zone (local shear rate 5 s^{-1}) of a suspension flowing into a square channel with smooth inner walls. The length of the track is ~2.3 s.

confocal rheoscope to perform simultaneous rheology and velocity profiling of soft materials.

6.1. 2D tracking of channel flows

We start with a 2D example, the characterization of pressure-driven channel flow of colloidal pastes. We used a $\phi \approx 0.63$ suspension of fluorescent PMMA spheres (radius $a = 1.3 \pm 0.1$ μm, from microscopy), suspended in a mixture of CHB and mixed decalin for refractive index and buoyancy matching. A pressure difference, ΔP, was applied to drive the suspension into the square channels (side $2b = 50$ μm, smooth inner walls). The flow across the full channel width was imaged in 2D at 107 frames per second (image size 44×58 μm^2, 256×320 pixels) at a depth of 17 μm from the lower surface. The images were collected at a distance corresponding to ~2000 particle diameters from the channel inlet where entry effects have died out and the flow has negligible x-dependence on a scale compared to image size. The particles are located in 2D with accuracy ~50 nm [20,77]. According to Eq. (3), distortion of the particle image becomes significant only for $V > V_{2D}^{max} \simeq 600$ μm/s, which exceeds the maximum velocities at which we are able to track the particle. Assuming uniform motion, the results in Section 5.2.2 suggest that Iterated Tracking fails for flow velocities $V > V^{max} = a \times f_{scan} \simeq 140$ μm/s, but in practice the limit is smaller due to the presence of large velocity gradients.

For the experiments considered here, the flow profiles consist of a central region of uniform velocity $V \simeq V_c$ and lateral zones adjacent to the channel walls where the shear is localized, Fig. 13. We have discussed the detailed physics elsewhere [15]. To comment briefly, we note that such a profile in itself, could be consistent with predictions from the rheology of yield stress fluids [92]. However, in contrast to yield stress fluid predictions, the velocity profiles scale with flow rate and the width of the shear zones is independent of flow rate [15]. By examining the microscopic dynamics of the particles we observe that they are dominated by interparticle collisions and contacts with similarities to dense granular flows. The similarities extend to the shape and scaling of the velocity profiles, which allowed to interpret the data using a stress fluctuation model initially conceived for dry grains [15].

In these experiments, the advected motion $\Delta X(y)$ is analyzed using Correlated Image Tracking with a scheme similar to that in Fig. 10(b). We divide the image in horizontal bins with sufficiently uniform displacements and obtain $\Delta X(y_q)$ from correlation in each of these. For channels with smooth walls, the particles near the wall are arranged in well defined layers, Fig. 13. Combined with the fact that velocity gradients are largest near the edge, this motivates the choice of one-particle-wide bins near the walls and a larger bin in the center. An example of the displacement profile $\Delta X(y_q, t_i)$ is shown in Fig. 13(b) and, combined with Eq. (7), can be used to track the particles in the CM frame. Fig. 14 shows a particle trajectory inside a shear zone both in the laboratory (left) and in the CM frame (right).

In Fig. 15(a),(b) we first show the displacement distribution functions for a small velocity $V_c \simeq 28$ μm/s (1.5 pixel/frame), for which particles can be tracked directly using classic CG tracking. These vanish smoothly within the tracking range and are consistent with the results (in the co-moving frame) from Iterated Tracking (open

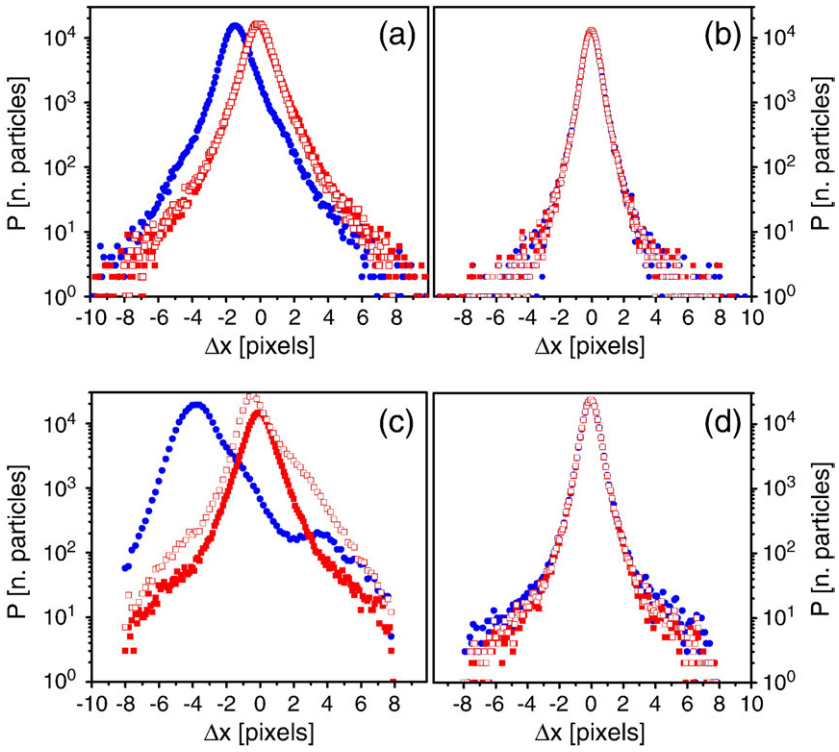

Fig. 15. Comparison of displacement distributions along x (a),(c) and y (b),(d) for 2D images of channel flow. Classic CG tracking in the laboratory frame (●), Iterated CG tracking (□), Correlated Image Tracking (■). (a),(b): slow flow ($V_c = -1.5$ pixel/frame); classic CG tracking is sufficient. (c),(d): fast flow ($V_c = -12$ pixel/frame). Here the classic CG tracking is inapplicable in the lab frame of reference (●), but Correlated Image Tracking utilizing CG tracking in the co-moving frame of reference is successful.

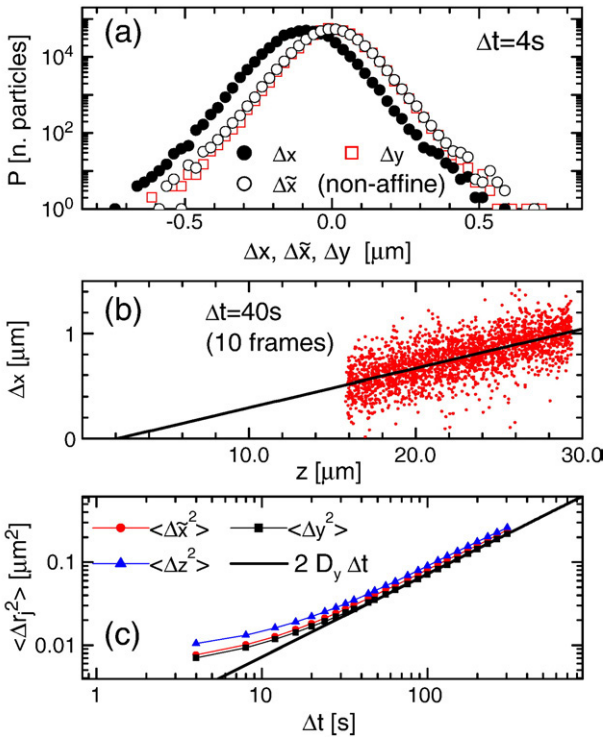

Fig. 16. Direct tracking of a sheared glass at $\dot{\gamma}=9.3\times10^{-4}$ s^{-1} (a) Histograms of frame to frame displacements. (b) Displacements Δx versus z for all particles over 10 frames ($\Delta t=40$ s). The line is a linear fit, the slope of which gives the local shear rate $\dot{\gamma}=9.3\times10^{-4}$ s^{-1}. (c) Mean squared displacement $\langle\Delta y^2(\Delta t)\rangle$ in the vorticity direction, $\langle\Delta z^2(\Delta t)\rangle$ in the gradient direction, and the non-affine MSD $\langle\Delta\tilde{x}^2(\Delta t)\rangle$ in the velocity direction. Line: $\langle\Delta y^2(\Delta t)\rangle=2D_y\Delta t$ with $D_y=3.6\times10^{-4}$ μm^2/s.

squares) and with the results from tracking in the CM frame, i.e. after removing non-uniform motion (filled squares).

For faster flow, $V_c\simeq223$ μm/s (~12 pixels/frame), Correlated Image Tracking is required. In Fig. 15(c) we show $P(\Delta x)$ from classic CG tracking (filled circles). The strong asymmetry and sharp cutoff show the inapplicability of this method. Results from iterative tracking, i.e. after removing uniform motion obtained from a preceding direct tracking step (open squares), still reveal asymmetry and are not reliable. Instead, the results from Correlated Image Tracking (full squares) are symmetric and show virtually no cut-off effects. The y-dependent motion after restoring these tracks to the laboratory frame are consistent with the advection profile $\Delta X(y)$ from correlation, confirming the success of the method. We note that for the different methods, the distributions $P(\Delta y)$, shown in Fig. 15(d), do not show any difference despite the variations observed in $P(\Delta x)$. This again illustrates that care must taken in interpreting displacement distribution functions from particle tracking as described in Section 5.1.

Finally, we also tested the method on ≃30% volume fraction suspensions in quasi-2D channels yielding the expected parabolic flow profiles [77,93]. With Correlated Image Tracking we have been able to successfully track particles in flows with velocity as high as 250 μm/s corresponding to almost twice the limit V^{max} mentioned above.

6.2. 3D particle tracking in simple shear flow

Next, we move to full 3D imaging and consider a colloidal glass in steady shear flow, measured in the rheometer or the shear cell with rough, coated surfaces. The apparatus has already been described in Section 3. The colloids (radius $a=850$ nm) are suspended in a charge-screened CHB–decalin mixture for refractive index and density matching ($\eta=2.6$ mPa·s). The volume fraction, measured from the average Voronoi volume determined from particle coordinates, is $\phi=0.62$. Each 3D image consists of 76 slices (256×256 pixels each, 2D frame rate $f=45$ s^{-1}), imaged over a height $z_{max}-z_0=15$ μm with z_0 either 10 μm or 15 μm ($z=0$ at the cover slide) and was acquired in ~1.7 s. The voxel size is $0.11\times0.11\times0.20$ μm^3. The local shear rate $\dot{\gamma}$ which we measure (see below) may exceed the overall applied rate $\dot{\gamma}_a$. This is due to global shear localization, which we observed directly in velocity profiles $v(z)$ measured from image series on a coarser z-scale, which we will describe in detail elsewhere [94].

The intrinsic accuracy for locating particles (with the refinement in [80]), obtained from the MSD in a random close packed system (no flow) is ±30 nm in x,y and ±70 nm in the z-direction. Under flow, using Eq. (3) in Section 4.2, the velocity for which distortion of the particle image sets in is $V_{3D}^{max}\sim1$ μm/s, exceeding our largest measured velocities $V_{3D}^{max}\sim\dot{\gamma}z_{max}$. The error due to short time thermal displacement is ±30 nm, not exceeding those mentioned above.

In Fig. 16 we show results for slow shear, where classic CG tracking is sufficient. Fig. 16(a) shows the distribution of frame to frame displacements along x (the velocity direction) and y (the vorticity direction). The former is shifted and slightly broader compared to $P(\Delta y)$ due to the z-dependence of ΔX and the zero-velocity plane being outside the image, which is illustrated by the displacement profile $\Delta x(z)$ (as obtained from the particle trajectories) in Fig. 16(b). The profile is linear on average on this z-scale, the slope gives the local shear rate $\dot{\gamma}=9.3\times10^{-4}$ s^{-1}, and it extrapolates to zero within experimental uncertainties at the cover-slide ($z=0$), confirming that the coating provides a stick boundary condition.

Locally, the shear induces plastic breaking of the particle cages, causing diffusive behavior at long times, as shown by the MSDs in Fig. 16(c) (see also [70]). This diffusion contrasts a *quiescent* colloidal glass where the long time particle dynamics remains caged. Fig. 16(c) includes the MSDs in the three directions x, y and z, where for the x direction we use $\langle\Delta\tilde{x}^2(t)\rangle$, with

$$\Delta\tilde{x}(t)=x(t)-x(0)-\dot{\gamma}\int_0^t z(t')\,dt', \tag{8}$$

which represents only the non-affine displacement. Note that with this definition, the usual effect of Taylor dispersion is suppressed, see e.g. [95]. As observed, the MSDs are nearly isotropic, i.e. the (non-affine) structural relaxation due to cage breaking is nearly the same for all directions [70]. The distribution of the non-affine displacements dx is also included in Fig. 16(a), and coincides with $P(\Delta y)$.

We now turn to faster shear, $\dot{\gamma}=0.019$ s^{-1}. We first consider a 2D image series taken at $z=18$ μm from the 3D stacks. From correlation we find a uniform motion with a constant velocity $V=1.6$ μm/frame. To

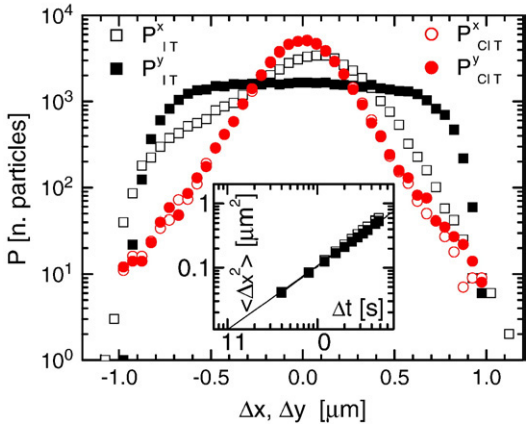

Fig. 17. Histograms of frame to frame displacements, in a comoving frame with $\langle\Delta x\rangle=0$, obtained from iterated CG tracking (P_{IT}, squares) and from Correlated Image Tracking (P_{CIT}, circles) for 2D imaging in the velocity vorticity plane of a sheared glass ($V=1.6$ μm/frame, $\dot{\gamma}=0.019$ s^{-1}). Inset: the MSD $\langle\Delta y^2(\Delta t)\rangle$ (■), and $\langle\Delta x^2(\Delta t)\rangle$ in the co-moving frame (□), from tracking in the CM frame. Line: $\langle\Delta y^2\rangle=2D_y\Delta t$ with $D_y=5.4\times10^{-5}$ μm^2/s.

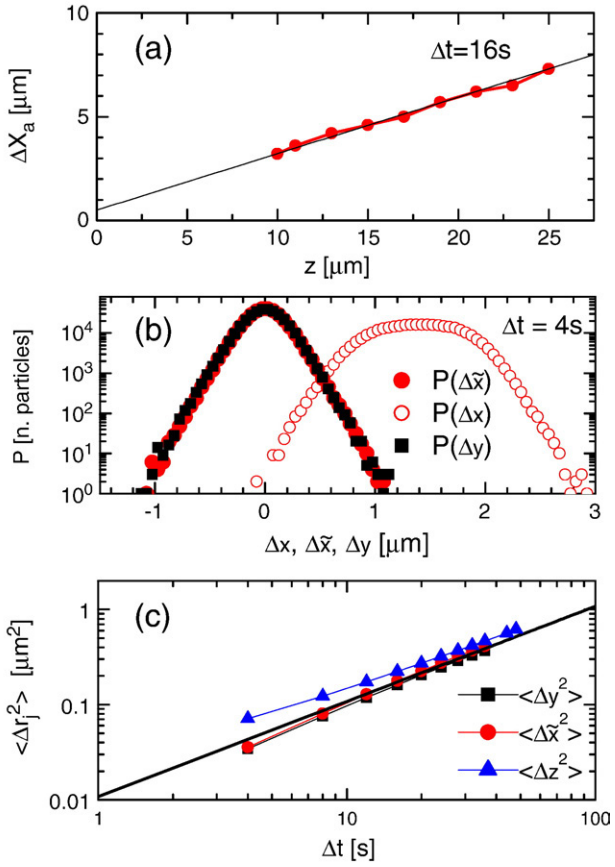

Fig. 18. 3D analysis of a sheared glass at $\dot{\gamma}=0.019\ s^{-1}$. (a) (●) accumulated displacement $\Delta X_a(z_r,t,\Delta t)$ from image correlation, for $t=40$ s over $\Delta t=16$ s (4 frames). Connecting lines represent the interpolating profile, defining $\Delta X_a(z,t,\Delta t)$. Line: linear fit giving an accumulated strain $d\Delta X_a/dz=0.28$. (b) Distribution of frame to frame displacements $P(\Delta x)$ and $P(\Delta y)$ after tracking in the CM frame ($R_T=1.1$ μm) and restoring the coordinates in the laboratory frame. Also shown is $P(\Delta x)$ of the non-affine x-displacements, using Eq. (8) and $\dot{\gamma}=0.019\ s^{-1}$. (c) the (non-affine) MSD in the three directions. The data are consistent with those in Fig. 17, inset. Line: $\langle\Delta y^2(\Delta t)\rangle=2D_y\Delta t$ with $D_y=5.4\times10^{-3}$ μm²/s.

compare with Section 5.2.2, using $\ell\sim1.8$ μm as the particle spacing, this corresponds to a reduced shift $s/\ell\simeq1$ between frames. We locate the particles in 2D, and track them both with iterated CG tracking, and with Correlated Image Tracking, using Eq. (7). In Fig. 17 the frame to frame displacement distributions from Iterated Tracking are shown, with $P(\Delta x)$ evaluated in a co-moving frame so that $\langle\Delta x\rangle=0$. These distributions are cut-off at $\Delta r=R_T=1$ μm by definition; the tracking program does not consider possible displacements larger than R_T (frame-to-frame). $P_{IT}(\Delta x)$ is asymmetric, similar to the MC data in Fig. 8(b).

This changes when we use Correlated Image Tracking and then examine the measured displacements in the co-moving frame. Now, the displacement distribution functions, Fig. 17, are no longer cut-off and coincide for Δy and Δx (in the co-moving frame), indicating correct tracking. The inset shows the resulting MSDs $\langle\Delta y^2(\Delta t)\rangle$ and $\langle\Delta\tilde{x}^2(\Delta t)\rangle$ (the latter again in the co-moving frame). As for slow shear, the dynamics is nearly isotropic. A more detailed description on the shear-induced structural relaxation is given in [70]. From the frame to frame MSD $\langle\Delta y^2(\Delta t=4\ s)\rangle\simeq0.05$ μm² we obtain $\langle\Delta r^2\rangle/\ell^2=\epsilon^2\simeq0.03$, within the limits for tracking in a concentrated quiescent system, Fig. 6.

To analyze the 3D data, we use Correlated Image Tracking where the correlation procedure is performed on image sequences at different heights $z_r=10+2r$ μm (r integer), as shown in Fig. 10(c). From this, we obtain the accumulated displacements profile $\Delta X_a(z_r,t,\Delta t)=\Sigma_{t-\Delta t}^{t}\Delta X(z_r,t)$, an example of which is shown in Fig. 18(a) for $t=40$ s and $\Delta t=16$ s. The profile is linear and again shows approximately stick boundary conditions. Time averages $\langle\Delta X_a(z_r,t,\Delta t=16\ s)\rangle_t$ (not shown) virtually overlap these data, showing that the flow is steady. To subtract this advected motion from the particle coordinates, we use the linear interpolation profile $\Delta X_a(z,t,\Delta t)$ shown by the lines connecting the symbols. Since both accumulated strain and non-affine displacements are large in this case, we performed both the subtraction of $\Delta X(z,t)$ (see Eq. (7)) and the "piecewise tracking", in intervals of 10 frames ($\Delta\gamma=80\%$), as described in Section 5.3.2. The resulting displacement distribution functions are shown in Fig. 18(b), both for the non-affine and the real displacements. Note the large range, $0\ \mu m\le\Delta x\le3$ μm, of the latter, resulting from the strong z gradient in advected motion. Finally, we show the MSDs for x, y and z calculated from these 3D data. The results for Δx^2 and Δy^2 match those in the inset to Fig. 17 while Δz^2 shows that despite the large shear rate, the dynamics remain nearly isotropic.

6.3. Rheology and velocity profiling

As a last example we describe the results of experiments on a more dilute colloidal suspension using the confocal rheoscope in cone plate geometry. Here we measure simultaneously the rheological response and map the velocity profile during flow, see Fig. 5.

The sample consists of a $\phi\sim55\%$ suspension of non-fluorescent PMMA-PHS colloids (radius=150 nm) in an index matching (decalin–tetralin) mixture, seeded with ~0.5% fluorescent tracers (radius=652 nm). Both the cone and the cover slide are coated with a layer of tracer particles. From the image series of the cone motion, we can verify the rotation speed of the rheometer during operation and by focusing on the top and bottom coatings we can map the spatial profile of the cone plate geometry. In Fig. 19 we show the variation of the gap size as function of the distance r from the center of the cone measured using the lateral objective translation. The truncation gap is nicely resolved and the data show that bending of the cover slide is negligible.

The velocity measurements were performed in two ways. One is the time-resolved mode: similarly to what is described in Section 6.2, we rapidly scan 3D stacks of ~20 to 50 slices, covering the entire gap from $z=0$ to $z=Z_{gap}=\theta r$ with θ the cone angle, Fig. 5(b). We use an oil-immersion objective with 200 μm working distance (60× magnification) and scan at equal speed both up and down to avoid disturbance of the sample due to large sudden displacements of the objective. By extracting the image series at each height and using the correlation method (Section 5.3.1), we obtain the time resolved displacements and shear profile. Typically it takes $\Delta t\sim1$ s to scan the gap. For the particular case of images containing tracers, displacements up to approximately half the image size S can be measured. Therefore, this mode is successful for maximum velocities $v\sim S/(2\Delta t)\sim50$ μm/s, with $S=100$ μm, which translates to $\dot{\gamma}_a r<S/(2\theta\Delta t)$. In the second mode ('stepping') we simply

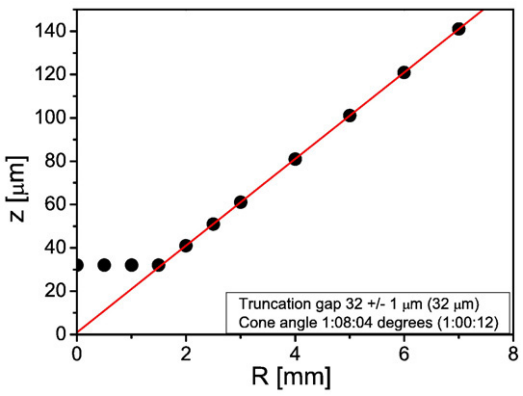

Fig. 19. Gap profile of the cone plate geometry, measured by confocal microscopy with fluorescent coating on both the bottom (glass) surface and the surface of the cone (radius 20 mm). The truncation gap is clearly visible and the profile extrapolates at zero height in the center. The nominal values of the truncation gap and of the cone angle are in brackets in the figure legend.

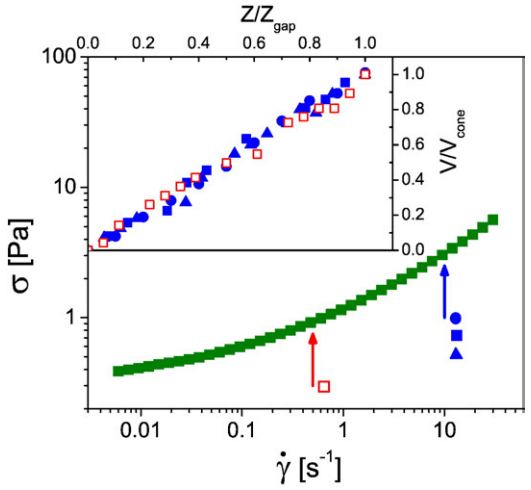

Fig. 20. Main panel: steady state stress σ versus applied shear rate $\dot{\gamma}$ for a $\phi \sim 55\%$ suspension of hard-sphere colloids of radius 150 nm. Inset: velocity profiles, normalized by the velocity of the cone V_{cone}, as a function of the height, normalized by the local gap size $Z_{gap} = \theta r$ of the geometry. Data for $\dot{\gamma} = 10\ s^{-1}$ are taken at different positions $r = 2.5$ mm (●), $r = 4$ mm (■) and $r = 5$ mm (▲) and for $\dot{\gamma} = 0.5\ s^{-1}$ data are taken at $r = 5$ mm (□).

record a time series at each z and reconstruct the velocity profile $v(z)$. Here the maximum velocity which can be measured is considerably larger: $v \sim S f_{scan}/2 \sim 5$ mm/s for $f_{scan} = 100\ s^{-1}$. This corresponds to a maximum shear rate of $\dot{\gamma} \sim 30\ s^{-1}$ for $r = 10$ mm. Note that even larger velocities can be measured by using smaller magnification objectives.

Fig. 20 (main panel) shows the steady state flow curve of the sample. Since the suspension at this volume fraction is in the proximity of the glass transition ($\phi_g \sim 57\%$), the expected low-rate Newtonian regime occurs at shear rates below our experimental window. In the regime we measured, $0.006\ s^{-1} < \dot{\gamma} < 30\ s^{-1}$ the sample exhibits strongly nonlinear rheology with pronounced shear thinning response (the viscosity decreases dramatically on increasing shear rate). In the inset we show some velocity profiles, measured in the 'stepping' mode at different shear rates and various distances r from the center of the cone. The corresponding gap sizes range from $Z_{gap} \simeq 50$ μm at $r = 2.5$ mm to $Z_{gap} \simeq 100$ μm at $r = 5$ mm. It is clear that the normalized profiles are linear, independent of $\dot{\gamma}$ and r. In the case of larger volume fractions, above the glass transition, $\phi > \phi_g$, we observe either slip or shear localization, depending on the boundary conditions. These results will be discussed in detail elsewhere [76,94].

7. Conclusion

In this paper we have described new instrumentation and analysis algorithms for 2D and 3D imaging studies of concentrated (colloidal) suspensions during flow. The combination of fast confocal microscopy and controlled flow, such as in a rheometer where simultaneous rheological information is available, opens up new horizons for the study of driven soft matter systems at high concentrations. Our evaluation of the CG tracking algorithm establishes the validity of previous experiments on colloidal dynamics. Finally, our method for particle tracking in a locally co-moving frame allows us to investigate the affine and non-affine dynamics of colloids during flow up to relatively large velocity (gradients), limited primarily by the amount of non-affine motion during flow. The method could therefore be of use in a variety of other applications, including the study of granular flow at single-particle level.

Acknowledgements

We thank N. Pham, J. Arlt and K.N. Pham for advice on the experiments and design of the confocal rheoscope, A.B. Schofield for particle synthesis, A. Garrie, A. Downie, and V. Devine for technical support, and E. Kim for providing the 3D Monte Carlo simulation data for hard-spheres. Eric R. Weeks thanks J.C. Crocker for helpful discussions over many years. R. Besseling and W.C.K. Poon acknowledge funding through EPSRC GR/S10377/01 and EP/D067650. L. Isa was funded by the EU network MRTN-CT-2003-504712. E.R. Weeks was funded through NSF DMR-0603055 (US).

References

[1] Pusey PN. In: Hansen JP, Levesque D, Zinn-Justin J, editors. Liquids, freezing and glass transition. Elsevier; 1991. p. 767–942. Ch. 10.
[2] Poon WCK, Pusey PN. In: Baus M, Full LF, Ryckaert JP, editors. Observation, prediction and simulation of phase transitions in complex fluids. Kluwer; 1995. p. 3–51. Ch. 1.
[3] Poon WCK. The physics of a model colloid–polymer mixture. J Phys Condens Mater 2002;14:R859–80.
[4] Aarts DGAL, Schmidt M, Lekkerkerker HNW. Interfacial dynamics in demixing systems with ultralow interfacial tension. Science 2004;304(5672):847–50.
[5] Anderson VJ, Lekkerkerker HNW. Insights into phase transition kinetics from colloid science. Nature 2002;416(6883):811–5.
[6] Dawson KA. The glass paradigm for colloidal glasses, gels, and other arrested states driven by attractive interactions. Curr Opin Colloid Interface Sci 2002;7:218–27.
[7] Sciortino F, Tartaglia P. Glassy colloidal systems. Adv Phys 2005;54:471–524.
[8] Zaccarelli E. Colloidal gels: equilibrium and non-equilibrium routes. J Phys Condens Mater 2007;19:323101.
[9] Fielding SM, Sollich P, Cates ME. Aging and rheology in soft materials. J Rheol 2000;44:323–69.
[10] Fuchs M, Cates ME. Theory of nonlinear rheology and yielding of dense colloidal suspensions. Phys Rev Lett 2002;89:248304.
[11] Kobelev V, Schweizer KS. Strain softening, yielding, and shear thinning in glassy colloidal suspensions. Phys Rev, E 2005;71:021401.
[12] Wilson DI, Rough SL. Exploiting the curious characteristics of dense solid–liquid pastes. Chem Eng Sci 2006;61:4147–54.
[13] Lewis JA. Colloidal processing of ceramics. J Am Ceram Soc 2000;83:2341–59.
[14] Jaeger HM, Nagel SR, Behringer RP. Granular solids, liquids, and gases. Rev Mod Phys 1996;68(4):1259–73.
[15] Isa L, Besseling R, Poon WCK. Shear zones and wall slip in the capillary flow of concentrated colloidal suspensions. Phys Rev Lett 2007;98(18):198305.
[16] Coussot P, Ancey C. Rheophysical classification of concentrated suspensions and granular pastes. Phys Rev, E 1999;59:4445–57.
[17] Lindner P, Zemb T, editors. Neutron X-rays & light: scattering methods applied to soft condensed matter. North Holland; 2002.
[18] Perrin JB. Atoms. London: Constable; 1916.
[19] Prasad V, Semwogerere D, Weeks ER. Confocal microscopy of colloids. J Phys Condens Mater 2007;19:113102.
[20] Crocker JC, Grier DG. Methods of digital video microscopy for colloidal studies. J Colloid Interface Sci 1996;179:298.
[21] Zahn K, Maret G. Dynamic criteria for melting in two dimensions. Phys Rev Lett 2000;85:3656–9.
[22] Zahn K, Wille A, Maret G, Sengupta S, Nielaba P. Elastic properties of 2D colloidal crystals from video microscopy. Phys Rev Lett 2003;90:155506.
[23] Ebert F, Keim P, Maret G. Local crystalline order in a 2D colloidal glass former. Eur Phys J, E 2008;26:161–8.
[24] Baumgartl J, Bechinger C. On the limits of digital video microscopy. Europhys Lett 2005;71:487–93.
[25] Elliot MS, Poon WCK. Conventional optical microscopy of colloidal suspensions. Adv Colloid Interface Sci 2001;92:133–94.
[26] Elliot MS, Bristol BTF, Poon WCK. Direct measurement of stacking disorder in hard sphere colloidal crystals. Physica A 1997;235:216–23.
[27] Wilson T. Confocal microscopy. San Diego: Academic Press; 1990.
[28] van Blaaderen A, Wiltzius P. Real-space structure of colloidal hard-sphere glasses. Science 1995;270(5239):1177–9.
[29] Dinsmore AD, Weeks ER, Prasad V, Levitt AC, Weitz DA. Three-dimensional confocal microscopy of colloids. App Optics 2001;40:4152–9.
[30] Habdas P, Weeks ER. Video microscopy of colloidal suspensions and colloidal crystals. Curr Opin Colloid Interface 2002;7:196–203.
[31] Semwogerere D, Weeks ER. Confocal microscopy, encyclopedia of biomaterials and biomedical engineering. Taylor & Francis; 2005.
[32] Gasser U, Weeks ER, Schofield A, Pusey PN, Weitz DA. Real-space imaging of nucleation and growth in colloidal crystallization. Science 2001;292:258–62.
[33] Kegel WK, van Blaaderen A. Direct observation of dynamical heterogeneities in colloidal hard-spheres suspensions. Science 2000;287:290–3.
[34] Weeks ER, Crocker JC, Levitt AC, Schofield A, Weitz DA. Three-dimensional direct imaging of structural relaxation near the colloidal glass transition. Science 2000;287:627–31.
[35] W.C.K. Poon, R. Besseling, L. Isa, A.B. Schofield, Imaging of hard-sphere colloids under flow, Adv. Polymer Sci. to be published.
[36] Pham KN, Petekidis G, Vlassopoulos D, Egelhaaf SU, Pusey PN, Poon WCK. Yielding of colloidal glasses. Europhys Lett 2006;75:624–30.
[37] Pham KN, Petekidis G, Vlassopoulos D, Egelhaaf SU, Poon WCK, Pusey PN. Yielding behavior of repulsion- and attraction-dominated colloidal glasses. J Rheol 2008;52:649–76.
[38] Russel W, Grant M. Distinguishing between dynamic yielding and wall slip in a weakly flocculated colloidal dispersion. Colloids Surf, A 2000;161:271.

[39] Buscall R, McGowan JI, Morton-Jones AJ. The rheology of concentrated dispersions of weakly attracting colloidal particles with and without wall slip. Colloids Surf, A 1993;37:621.
[40] Olmsted PD. Perspectives on shear banding in complex fluids. Rheol Acta 2008;47:283–300.
[41] Raffel M, Willert C, Kompenhans J. Particle image velocimetry, a practical guide. Berlin: Springer; 1998.
[42] Meeker SP, Bonnecaze RT, Cloitre M. Slip and flow in soft particle pastes. Phys Rev Lett 2004;92(19):198302.
[43] Meeker SP, Bonnecaze RT, Cloitre M. Slip and flow in pastes of soft particles: direct observation and rheology. J Rheol 2004;48(6):1295–320.
[44] Salmon JB, Manneville S, Colin A, Pouligny B. An optical fiber based interferometer to measure velocity profiles in sheared complex fluids. Eur Phys J, Appl Phys 2003;22:143.
[45] Manneville S, Bécu L, Colin A. High-frequency ultrasonic speckle velocimetry in sheared complex fluids. Eur Phys J, Appl Phys 2004;28:361.
[46] Bécu L, Manneville S, Colin A. Yielding and flow in adhesive and nonadhesive concentrated emulsions. Phys Rev Lett 2006;96(13):138302.
[47] Bécu L, Anache D, Manneville S, Colin A. Evidence for three-dimensional unstable flows in shear-banding wormlike micelles. Phys Rev, E 2007;76(1):011503.
[48] Fukushima E. Nuclear magnetic resonance as a tool to study flow. Annu Rev Fluid Mech 1999;31:95–123 and references therein.
[49] Callaghan PT. Rheo-NMR: nuclear magnetic resonance and the rheology of complex fluids. Rep Progr Phys 1999;62(4):599–670.
[50] Bonn D, Rodts S, Groenink M, Rafaï S, Shahidzadeh-Bonn N, Coussot P. Some applications of magnetic resonance imaging in fluid mechanics: complex flows and complex fluids. Annu Rev Fluid Mech 2008;40:209–33.
[51] Gladden LF, Alexander P. Applications of nuclear magnetic resonance imaging in process engineering. Meas Sci Technol 1996;7(3):423–35.
[52] Ovarlez G, Bertrand F, Rodts S. Local determination of the constitutive law of a dense suspension of noncolloidal particles through magnetic resonance imaging. J Rheol 2006;50(3):259–92.
[53] Raynaud JS, Moucheront P, Baudez JC, Bertrand F, Guilbaud JP, Coussot P. Direct determination by nuclear magnetic resonance of the thixotropic and yielding behavior of suspensions. J Rheol 2002;46(3):709–32.
[54] Huang N, Ovarlez G, Bertrand F, Rodts S, Coussot P, Bonn D. Flow of wet granular materials. Phys Rev Lett 2005;94:028301.
[55] Fall A, Huang N, Bertrand F, Ovarlez G, Bonn D. Shear thickening of cornstarch suspensions as a reentrant jamming transition. Phys Rev Lett 2008;100(1):018301.
[56] Breedveld V, van den Ende D, Tripathi A, Acrivos A. The measurement of the shear-induced particle and fluid tracer diffusivities in concentrated suspensions by a novel method. J Fla Mech 1998;375:297.
[57] Breedveld V, van den Ende D, Bosscher M, Jongschaap RJJ, Mellema J. Measuring shear-induced self-diffusion in a counterrotating geometry. Phys Rev, E 2001;63:021403.
[58] Haw MD, Poon WCK, Pusey PN. Direct observation of oscillatory-shear-induced order in colloidal suspensions. Phys Rev, E 1998;57(6):6859–64.
[59] Haw MD, Poon WCK, Pusey PN, Hebraud P, Lequeux F. Colloidal glasses under shear strain. Phys Rev, E 1998;58(4):4673–82.
[60] Smith P, Petekidis G, Egelhaaf SU, Poon WCK. Yielding and crystallization of colloidal gels under oscillatory shear. Phys Rev, E 2007;76:041402.
[61] Biehl R, Palberg T. Modes of motion in a confined colloidal suspension under shear. Europhys Lett 2004;66(2):291–5.
[62] Tolpekin VA, Duits MHG, van den Ende D, Mellema J. Aggregation and breakup of colloidal particle aggregates in shear flow, studied with video microscopy. Langmuir 2004;20(7):2614–27.
[63] Hoekstra H, Vermant J, J M. Flow-induced anisotropy and reversible aggregation in two-dimensional suspensions. Langmuir 2003;21(24):9134–41.
[64] Stancik EJ, Gavranovic GT, Widenbrant MJO, Laschtisch AT, Vermant J, Fuller GG. Structure and dynamics of particle monolayers at a liquid–liquid interface subject to shear flow. Faraday Discuss 2003;123:145–56.
[65] Varadan P, Solomon MJ. Direct visualization of flow-induced microstructure in dense colloidal gels by confocal laser scanning microscopy. J Rheol 2003;47(4):943–68.
[66] Cohen I, Mason T, Weitz D. Shear-induced configurations of confined colloidal suspensions. Phys Rev Lett 2004;93:046001.
[67] Solomon T, Solomon MJ. Stacking fault structure in shear-induced colloidal crystallization. J Chem Phys 2006;124(13):134905.
[68] Derks D, Wisman H, van Blaaderen A, Imhof A. Confocal microscopy of colloidal dispersions in shear flow using a counter-rotating cone plate shear cell. J Phys Condens Mater 2004;16:S3917–27.
[69] Wu YL, Brand JHJ, van Gemert JLA, Verkerk J, Wisman H, van Blaaderen A, Imhof A. A new parallel plate shear cell for *in situ* real-space measurements of complex fluids under shear flow. Rev Sci Instrum 2007;78:103902.
[70] Besseling R, Weeks ER, Schofield AB, Poon WCK. Three-dimensional imaging of colloidal glasses under steady shear. Phys Rev Lett 2007;99:028301.
[71] Xu H, Reeves AP, Louge MY. Measurement error in the mean and fluctuation velocities of spherical grains form a computer analysis of digital images. Rev Sci Instrum 2004;75(4):811–9.
[72] Antl L, Goodwin JW, Hill RD, Ottewill RH, Owens SM, Papworth S, Waters JA. The preparation of poly(methyl methacrylate) lattices in non-aqueous media. Colloids Surf 1986;17(1):67–78.
[73] Ackerson BJ, Pusey PN. Shear-induced order in suspensions of hard-spheres. Phys Rev Lett 1988;61(8):1033–6.
[74] Yethiraj A, van Blaaderen A. A colloidal model system with an interaction tunable from hard sphere to soft and dipolar. Nature 2003;421(6922):513–7.
[75] Lu PJ, Conrad JC, Wyss HM, Schofield AB, Weitz DA. Fluids of clusters in attractive colloids. Phys Rev Lett 2006;96:028306.
[76] P. Ballesta, R. Besseling, L. Isa, G. Petekidis, W.C.K. Poon, arXiv:0807.1437v1 (2008).
[77] Isa L, Besseling R, Weeks ER, Poon WCK. Experimental studies of the flow of concentrated hard sphere suspensions into a constriction. J Phys Conf Series 2006;40:124–32.
[78] E.R. Weeks, J.C. Crocker, Particle tracking using IDL: website, http://www.physics.emory.edu/~weeks/idl/.
[79] Brangwynne CP, Koenderink GH, Barry E, Dogic Z, MacKintosh FC, Weitz DA. Bending dynamics of fluctuating biopolymers probed by automated high-resolution filament tracking. Biophys J 2007;93:346–59.
[80] Jenkins M, Egelhaaf SU. Confocal microscopy of colloidal particles: towards reliable, optimum coordinates. Adv Colloid Interface Sci 2008;136(1–2):65–92.
[81] Pusey PN, Tough RJA. Hydrodynamic interactions and diffusion in concentrated particle suspensions. Faraday Discuss 1983;76(76):123–36.
[82] Beenhakker C, Mazur P. Diffusion of spheres in a concentrated suspension.2. Physica A 1984;126:349–70.
[83] Tokuyama M, Oppenheim I. Dynamics of hard-spheres suspensions. Phys Rev, E 1994;50:R16.
[84] Brady J. Brownian-motion, hydrodynamics, and the osmotic-pressure. J Chem Phys 1993;567:99.
[85] van Megen W, Mortensen TC, Williams SR, Müller J. Measurements of the self-intermediate scattering function of suspensions of hard spherical particles near the glass transition. Phys Rev, E 1998;58(5):6073–85.
[86] Steager E, Kim CB, Patel J, Bith S, Naik C, Reber L, Kim MJ. Control of microfabricated structures powered by flagellated bacteria using phototaxis. Appl Phys Lett 2007;90:263901.
[87] Rogers SS, Waigh TA, Lu JR. Intracellular microrheology of motile amoeba proteus. Biophys J 2008;94(8):3313–22.
[88] Chetverikov D. Particle image velocimetry by feature tracking. Lect Notes in Comput Sci 2001;2124:325.
[89] Doliwa B, Heuer A. Cage effect, local anisotropies, and dynamic heterogeneities at the glass transition: a computer study of hard spheres. Phys Rev Lett 1998;80:4915.
[90] Jaster A. Orientational order of the two-dimensional hard-disk system. Europhys Lett 1998;277.
[91] Habdas P, Schaar D, Levitt AC, Weeks ER. Forced motion of a probe particle near the colloidal glass transition. Europhys Lett 2004;67(3):477–83.
[92] Huilgol RR, You Z. Application of the augmented Lagrangian method to steady pipe flows of Bingham, Casson and Herschel–Bulkley fluids. J Non-Newton Fluid Mech 2005;128:126–43.
[93] Frank M, Anderson D, Weeks ER, Morris JF. Particle migration in pressure-driven flow of a Brownian suspension. J Fluid Mech 2003;493:363–78.
[94] R. Besseling, P. Ballesta, L. Isa, G. Petekidis, W.C.K. Poon, Shear localization in hard-sphere colloidal glasses, in preparation.
[95] Yamamoto R, Onuki A. Dynamics of highly supercooled liquids: heterogeneity, rheology, and diffusion. Phys Rev, E 1998;58(3):3515–29.